

Electronic Theses and Dissertations, 2004-2019

2017

Mechanism of Actin Bundle Assembly, Mechanics and Structure by Ion Interaction

Nicholas Castaneda
University of Central Florida

 Part of the [Nanoscience and Nanotechnology Commons](#)
Find similar works at: <https://stars.library.ucf.edu/etd>
University of Central Florida Libraries <http://library.ucf.edu>

This Masters Thesis (Open Access) is brought to you for free and open access by STARS. It has been accepted for inclusion in Electronic Theses and Dissertations, 2004-2019 by an authorized administrator of STARS. For more information, please contact STARS@ucf.edu.

STARS Citation

Castaneda, Nicholas, "Mechanism of Actin Bundle Assembly, Mechanics and Structure by Ion Interaction" (2017). *Electronic Theses and Dissertations, 2004-2019*. 5446.
<https://stars.library.ucf.edu/etd/5446>

**MECHANISM OF ACTIN BUNDLE ASSEMBLY, MECHANICS
AND STRUCTURE BY ION INTERACTION**

by

NICHOLAS CASTANEDA
B.S. Florida International University, 2015

A thesis submitted in partial fulfillment of the requirements
for the degree of Master of Science
in the NanoScience Technology Center
in the College of Graduate Studies
at the University of Central Florida
Orlando, Florida

Spring Term
2017

Major Professor: Hyeran Kang

© 2017 Nicholas Castaneda

ABSTRACT

The assembly of actin filaments into bundles plays an essential role in mechanical strength and dynamic reorganization of cytoskeleton. Divalent counterions at high concentrations promote bundle formation through electrostatic attraction between charged filaments. Although it has been hypothesized that specific cation interactions may contribute to salt-induced bundling, molecular mechanisms of how salt modulates bundle assembly and mechanics are not well established. Here we determine the mechanical and dynamic properties of actin bundles with physiologically relevant cations. Using total internal reflection fluorescence (TIRF) microscopy, we measure the bending stiffness of actin bundles determined by persistence length analysis. We characterize real-time formation of bundles by dynamic light scattering intensity and direct visualization using TIRF microscopy. Our results show that divalent cations modulate bundle stiffness as well as time-dependent average bundle size. Furthermore, molecular dynamic simulations propose specificity for cation binding on actin filaments to form bundles. The work suggests that cation interactions serve a regulatory function in bundle assembly dynamics, mechanics, and structure.

Keywords: polyelectrolyte, persistence length, bundle-specific cation binding

ACKNOWLEDGMENTS

This thesis would not have been possible without the support of many, mainly my thesis chair and mentor, Dr. Hyeran Kang, who read my numerous revisions and helped me understand what it takes to become a scientist and a leader. Also, I would like to thank my committee members, Dr. Qun Huo, and Dr. Andre Gesquiere, who offered guidance and support. In addition, the research performed for this thesis was an inclusive effort conveyed by many incredible scientific minds and talents. I would like to thank Tianyu Zheng and his mentor Dr. Qun Huo, who have guided and mentored me throughout the dynamic light scattering (DLS) experimentations. Through their insight and knowledge, we were able to understand the dynamic nature of the actin bundle system. I would like to thank our collaborators Dr. Hyun Joo Lee and Dr. Jaekyung Hyun at KBSI for your transmission electron microscopy (TEM) work that allowed for the advancement of our understanding of actin bundling. I would like to thank Dr. Hector Rivera-Jacquez and Dr. Alexander Balaeff for their incredible work on molecular dynamic simulations. It was through the guidance and patience of Dr. Rivera-Jacquez that I could learn the proper techniques and experimental protocols associated to our actin system. I would like to thank my lab members for their support and assistance during the experimental process and analysis. Additionally, I want to thank the University of Central Florida and NanoScience Technology Center for awarding me the opportunity to express my fullest potential in the realm of scientific knowledge. Lastly, thank you to my parents, and numerous friends who endured this long process with me, always offering love and support. Their advice and direction has been invaluable throughout this entire process and their words of encouragement created a platform for me to build a memorable future upon.

TABLE OF CONTENTS

LIST OF FIGURES	vii
LIST OF ACRONYMS (or) ABBREVIATIONS	viii
CHAPTER ONE: INTRODUCTION.....	1
1.1 Actin Cytoskeleton.....	1
1.1.1 Actin Monomer and Filament Structure.....	1
1.1.2 Actin Filament Assembly and Mechanics	3
1.2 Bundle Assembly and Mechanics	4
1.2.1 Bundles Induced by Cross-linking Proteins	4
1.2.2 Cation-Induced Bundles	5
1.3 Hypothesis.....	7
CHAPTER TWO: MATERIALS AND METHODS	11
2.1 Protein and Sample Preparations.....	11
2.2 Sedimentation Assay.....	11
2.3 TIRF Microscopy Imaging.....	12
2.4 Actin Bundle Persistence Length (L_p) and Average Length Analysis	12
2.5 TEM Imaging and Bundle Thickness Analysis.....	13
2.6 Time-Dependent Bundle Fluorescence Analysis	14
2.7 Dynamic Light Scattering (DLS)	14

2.8 Molecular Dynamics Simulation.....	15
CHAPTER THREE: RESULTS	17
3.1 Divalent Cations Modulate Bundle Mechanics and Size Distribution.....	17
3.2 Divalent Cations Modulate Bundle Thickness.....	18
3.3 Visualization of Time-Dependent Bundle Formation.....	18
3.4 Scattering Intensity Determines Actin Bundle Assembly Dynamics.....	19
3.5 Specific Cation Binding Modulates Actin Bundle Formation	20
CHAPTER FOUR: DISCUSSION.....	29
CHAPTER FIVE: CONCLUSION.....	34
APPENDIX A: DETERMINATION OF ACTIN BUNDLE PERSISTENCE LENGTH.....	36
APPENDIX B: LOW-SPEED SEDIMENTATION INDICATES PERCENTAGE OF BUNDLES PER SALT CONDITION	38
APPENDIX C: MONOVALENT CATIONS AFFECT ACTIN FILAMENT ASSEMBLY.....	40
APPENDIX D: DIAMETER ANALYSIS OF TEM IMAGES	42
APPENDIX E: TIME-DEPENDENT IMAGES CORRELATE TO ACTIN BUNDLE LENGTHS	44
APPENDIX F: DYNAMIC BUNDLE FORMATION AT LOW ACTIN CONCENTRATION.....	46
REFERENCES	48

LIST OF FIGURES

Figure 1. Representation of actin polymerization in presence of salt.....	8
Figure 2. Elongation of actin filament and ATP hydrolysis with dissociation of phosphate	9
Figure 3. Schematic representation of actin filament modulation by multivalent counterions	10
Figure 4. Cation induced polymerization affects actin bundle mechanics	23
Figure 5. TEM imaging displays modulation of bundles by divalent cations	24
Figure 6. Time-dependent average length and fluorescence of bundles.....	25
Figure 7. DLS indicates kinetic and thermodynamic polymerization of actin bundles	26
Figure 8. Structural dynamics of simulated actin bundle	27
Figure 9. Cations and actin subdomain interactions form bundles.....	28
Supplemental Figure 1. Determination of actin bundle persistence length	37
Supplemental Figure 2. Low-speed sedimentation indicates percentage of bundles per salt condition	39
Supplemental Figure 3. Monovalent cations affect actin filament assembly	41
Supplemental Figure 4. Diameter analysis of TEM images	43
Supplemental Figure 5. Time-dependent images correlate to actin bundle lengths	45
Supplemental Figure 6. Dynamic bundle formation at low actin concentration	47

LIST OF ACRONYMS (or) ABBREVIATIONS

< C(s) >	Average Angular Correlation
1D	One Dimensional
ABP	Actin Binding Protein
ADP	Adenosine Di-Phosphate
ADP + P _i	Adenosine Di-Phosphate + Phosphate
APD	Avalanche Photodiode
ASP	Aspartic Acid
ATM	Atmospheric Pressure
ATP	Adenosine Tri-Phosphate
B _D	Bundle Diameter
Buffer A	Actin Storage Buffer
CaI	Calcium Chloride and Imidazole Buffer
C _c	Critical Concentration
CCD	Charged Coupled Device
CDW	Charge Density Wave
CHARMM	Chemistry at HARvard Molecular Mechanics Simulation Program
CMAP	Cross-term for Dihedral Angles of Protein Backbones
DB-loop	DNase I Binding Loop
ddH ₂ O	Double Deionized Water
DLS	Dynamic Light Scattering
D _p	Diameter of Pixel
DTT	Dithiothreitol
EGTA	Ethylene glycol-bis(β-aminoethyl ether)-N,N,N',N'-tetraacetic acid
EM	Electron Microscopy
G-Actin	Globular Actin
GLU	Glutamic Acid
F-Actin	Filamentous Actin
Fs	Femtosecond
κ	Flexural Rigidity
K _B	Boltzmann's constant
kcps	Kilo Count per Second
KI	Potassium Chloride and Imidazole Buffer
L _p	Persistence Length
MD	Molecular Dynamics
MEAD	Macroscopic Electrostatics with Atomic Detail Program
MI	Magnesium Chloride and Imidazole Buffer
NaI	Sodium Chloride and Imidazole Buffer
NAMD	Nanoscale Molecular Dynamics Program
NPT	Normal Pressure and Temperature
Ns	Nanosecond
PAGE	Polyacrylamide Gel Electrophoresis
Ps	Picosecond

Rho	Rhodamine Labeled
RNA	Ribonucleic Acid
SD	Subdomain
SDS	Sodium Dodecyl Sulfate
SE	Standard Error
S_p	Scale Bar in Pixels
T	Temperature
TEM	Transmission Electron Microscopy
TIP3P	Simulated Water Model
TIRF	Total Internal Reflection Fluorescence
VMD	Visual Molecular Dynamics

CHAPTER ONE: INTRODUCTION

The following chapter intends to inform the reader on the basics of the actin structure and function, and how actin assembly dynamics and mechanics are regulated. Actin is an essential protein of living cells and its dysfunctions are linked to many diseases. The central theme of this thesis is to suggest molecular mechanisms of structural, mechanical and dynamic properties for actin bundles modulated by specific ion interactions.

1.1 Actin Cytoskeleton

Actin cytoskeleton is the essential component of cell mechanics and organization, and dynamic fluctuations of the cytoskeleton is greatly influenced by cellular mechanical responses to external stimuli (De La Cruz & Gardel, 2015; Dos Remedios et al., 2003; Pollard & Cooper, 2009). Actin plays a critical role in cell motility, force generation, signal transduction, neuronal synapse contacts, and cell division (Fernandez-Valle, Gorman, Gomez, & Bunge, 1997; Fletcher & Mullins, 2010; Lieleg, Kayser, Brambilla, Cipelletti, & Bausch, 2011; Pollard & Cooper, 2009; Yang et al., 2007). In addition, along the outer edges of the cell membrane, filopodia composed of actin bundles allow for movement and extracellular environmental interactions.

1.1.1 Actin Monomer and Filament Structure. The molecular weight of G-actin is ~42kDa and ~375 amino acids in length (Dos Remedios et al., 2003). A nucleotide cleft can be found in the center of G-actin structure, usually occupied by a bound ATP, ADP+P_i or ADP separating subdomains 1-2 and 3-4 (Figure. 1) (De La Cruz & Gardel, 2015; Dos Remedios et al., 2003). The ATP bound to the nucleotide cleft can generate a complex with either Ca²⁺ or Mg²⁺ *in vivo*, which allows for an opening and closing of the nucleotide cleft (De La Cruz & Gardel, 2015;

Dos Remedios et al., 2003). Monomer-monomer interactions occur at designated areas on the G-actin structure.

The “pointed-end” and “barbed-end” are located on opposing sides of the monomer structure (Dos Remedios et al., 2003), corresponding with G-actin dissociation and association, respectively (De La Cruz & Gardel, 2015; Pollard & Cooper, 2009). Another major structure associated to G-actin is DNase I binding loop (DB-loop) (De La Cruz & Gardel, 2015; Kang et al., 2012). The DB-loop is comprised of amino acid residues within subdomain 2, and is responsible for the monomer-monomer contacts within the filament. The interactions coincide with the DB-loop and subdomain 3 of the adjacent monomer, thereby controlling filament stiffness (De La Cruz, Roland, McCullough, Blanchoin, & Martiel, 2010; Kang et al., 2012).

Actin monomers polymerize into filaments that are double stranded, helical biopolymers in the presence of salt in solution (Figure. 1). Recently, F-actin structure has been resolved by high-resolution electron cryomicroscopy (Fujii, Iwane, Yanagida, & Namba, 2010; Galkin, Orlova, Vos, Schroder, & Egelman, 2015) The structure of actin filament (F-actin) includes 13 monomers in 6 turns with the helix repeating every 37 subunits, a total rise of 27.3 Å, rotation of 166.15° on average, and a diameter of ~6-8nm (De La Cruz & Gardel, 2015; Fujii et al., 2010). Recent studies demonstrate that F-actin adopts multiple structural states (stated as “polymorphism” (Galkin, Orlova, Schroder, & Egelman, 2010; Galkin et al., 2015) with variable twist. Interactions between monomers occur along the diameter of the filament and mechanical properties of the filament are influenced by actin binding proteins (ABPs) interaction and/or surrounding environment such as salt concentrations or molecular crowding (Kang et al., 2014; Kang, Bradley, Elam, & De La Cruz, 2013; Rosin, Schummel, & Winter, 2015; Tang & Janmey, 1996).

1.1.2 Actin Filament Assembly and Mechanics. Through the binding of ATP, numerous G-actin spontaneously assemble to form actin filaments (Figure. 2) . The polymerization process begins slowly with monomer assembly forming a stable trimer structure (Dos Remedios et al., 2003; Pollard & Cooper, 2009). The formation of the trimer embodies a nucleus to which additional monomers are permitted to bind, thus initiating the elongation phase (Dos Remedios et al., 2003; Tobacman & Korn, 1983). The elongation phase occurs at the barbed end of the filament and dissociation of monomers ensues at the pointed end. The hydrolysis of ATP is what allows for the dissociation of monomers and subsequent release of ADP + P_i however, dissociated actin monomers in solution may exchange their bound ADP for ATP in order to maintain binding and replicate further (Dos Remedios et al., 2003; Tobacman & Korn, 1983). In addition, ion concentrations in solution have a profound effect on filament assembly, as well as the bound nucleotide and divalent cations (Kang et al., 2012).

Actin filament has bending stiffness compared to that of commercial plastics (Young's modulus of ~2GPa), allowing for inter-subunit interactions to sustain forces associated to movement and external force stimulation (Howard, 2001). The mechanical properties of actin filaments are determined by inter-subunit interactions that exhibit resistance to bending, twisting deformation, or twist-bend coupling (De La Cruz & Gardel, 2015; De La Cruz et al., 2010). Inside a cell, many ABPs and/or environmental factors regulate filament mechanics. For example, the forces generated by filament polymerization are capable of propelling the crawling motion of cells and influences their interactions with the extracellular environment (Pollard & Cooper, 2009), thereby indicating the physiological importance of filament polymerization on eukaryotic cells.

1.2 Bundle Assembly and Mechanics

The crosslinking of F-actin is an important stage in cell processes such as cell motility and filopodia generation. *In vivo*, bundle structures can occur through molecular crowding, ABPs and electrostatic interactions (Angelini et al., 2005; Goverman, Schick, & Newman, 1996; Jansen et al., 2011). Previous reports have suggested the use of ABPs in bundling F-actin to modulate mechanical properties (Claessens, Bathe, Frey, & Bausch, 2006; Jansen et al., 2011; Takatsuki, Bengtsson, & Mansson, 2014; Winkelman et al., 2016). Flexural rigidity, the amount of resistance presented by a structure undergoing bending, depends on the amount of filaments in a bundle and the effectiveness of the cross-linker. (Bathe, Heussinger, Claessens, Bausch, & Frey, 2008). Meanwhile, persistence length (L_p), a fundamental mechanical measurement of stiffness for a polymer, provides the quantitative data necessary for interpreting polymer bending rigidity (Graham et al., 2014). Therefore, filament cross-linking proteins and ionic electrostatic interactions provide possible modalities that can influence the mechanics associated with bundle assembly and overall structural dynamics (Tang & Janmey, 1996).

1.2.1 Bundles Induced by Cross-linking Proteins. Actin filaments cross-linked by various ABPs differ in their structural properties, bending flexibility and resistance to shear stress. As a result, some ABPs are concentration dependent in their cross-linking effectiveness elucidating a limitation for bundling, while others are capable of cross-linking independent of their protein concentration. For example, fimbrin is capable of cross-linking filaments into bundle assemblies independent of concentration (Bathe et al., 2008). On the other hand, fascin, a fairly abundant protein, is concentration dependent but maintains the ability to cross-link bundles efficiently and with substantial resistance to shear forces (Claessens et al., 2006). However, this concentration

dependency introduces a limitation on bundle size, as well as packing density (Stokes & DeRosier, 1991; Takatsuki et al., 2014). All in all, the fascin bundle packing density is limited to roughly ~20 filaments per bundle. Yet, due to inherent protein modulation, observed helical twisting of the bundle for conservation of energy is observed (Claessens et al., 2006; Claessens, Semmrich, Ramos, & Bausch, 2008; Jansen et al., 2011). These mechanisms are necessary to resist sheer forces and can be illustrated *in vivo*, predominately in filopodia and neurosensory bristles which are under high sheer stress and external stimuli (Bathe et al., 2008).

1.2.2 Cation-Induced Bundles. Actin filaments are charged biopolymers with $4e^-/nm$, and have potential to attract one another in the presence of multivalent cations (Fazli, Mohammadinejad, & Golestanian, 2009; Tang & Janmey, 1996). At relatively high concentrations, multivalent ions promote actin bundle formation through electrostatic attraction and van der waals forces (Figure. 3 A and B) (Angelini, Liang, Wriggers, & Wong, 2003; Fazli et al., 2009; Lai, Coridan, Zribi, Golestanian, & Wong, 2007; Tang, Ito, Tao, Traub, & Janmey, 1997; Tang & Janmey, 1996). Counterions of higher valence have a corresponding binding affinity which leads to charged actin filaments becoming neutralized (Tang & Janmey, 1996). The neutralization allows for electrostatic attractive interactions induced by two or more filaments sharing counterions to form bundle structures (Angelini et al., 2003). Light scattering studies have shown bundle formation to be threshold dependent with divalent cation concentrations (Figure. 3C) (Tang & Janmey, 1996). The concentration of cations necessary for bundling increases with decreased valence, thus indicating a substantial weakening of filament aggregation (Tang & Janmey, 1996). Trivalent cations are capable of bundling actin filaments at lower concentrations due to high valence (Korkmaz Zirpel & Park, 2015), while divalent and monovalent cations require greater amounts of ionic concentrations (Tang & Janmey, 1996; Yu

& Carlsson, 2003). However, the implications of divalent cation-induced bundling mechanics, structural dynamics and bending flexibility has not yet become apparent.

Development of bundles is theorized to be mediated by both electrostatic interactions and specific ion binding locations. However, discrete ion binding may in fact dominate filament mechanics, therefore governing the electrostatic screening effects. Current research suggests that site-specific cation binding does occur at discrete locations on actin filaments and as a result, controls assembly and the mechanics (Kang et al., 2013; Kang et al., 2012). Elucidating this fact, site-specific substitution of charged amino acids on filaments have already demonstrated regulation of polymerization and stiffness (Kang et al., 2012). However, divalent cation concentrations are capable of bundle formation only after surpassing what is required for polymerization (Tang & Janmey, 1996). Although filament mechanics are known to be influenced by ion binding at the DB-loop in SD2 (Kang et al., 2012), the mechanism of how ions modulate bundle mechanics is unclear.

Bundles with relatively high stiffness induced by divalent cations have proven limitations to size and growth, but promote structural deformation and contain high packing densities of filaments through short range steric interactions (Angelini et al., 2003; Henle & Pincus, 2005; Lai et al., 2007). The limitation of size and growth are in accordance to the concentration of divalent cations in solution (Henle & Pincus, 2005). Structural modulation is evident through helical twisting of filaments in response to variations in cation concentrations, as previously seen (Angelini et al., 2003). The ions surrounding the filaments form 1D charge density waves (CDW) parallel to the actin filaments, which lead to a twisting distortion (Angelini et al., 2003). The adjustment in geometry stimulates the filament to contain negatively charged evenly spaced

regions, assembling filaments in a parallel arrangement which may optimize their electrostatic interactions (Angelini et al., 2003). In addition, the packing density of filaments within a bundle are affected by inter-filament spacing determined by the cross-linker diameter, the amount of time bundling is allotted, and salt concentration (Lai et al., 2007; Winkelman et al., 2016).

1.3 Hypothesis

Electrostatic screening, counterion condensation and discrete ion binding influence the size, growth, structural dynamics and mechanics of filament formation. However, it is not entirely understood if discrete binding sites under high divalent ionic conditions contribute to the formation and mechanical properties associated to actin bundling. We hypothesize that specific cation binding modulates the mechanical, structural and dynamic properties of actin bundles. To test our hypothesis, we investigate the effects of cations on bundle assembly, mechanics, and structure through biophysical studies and molecular dynamics simulation.

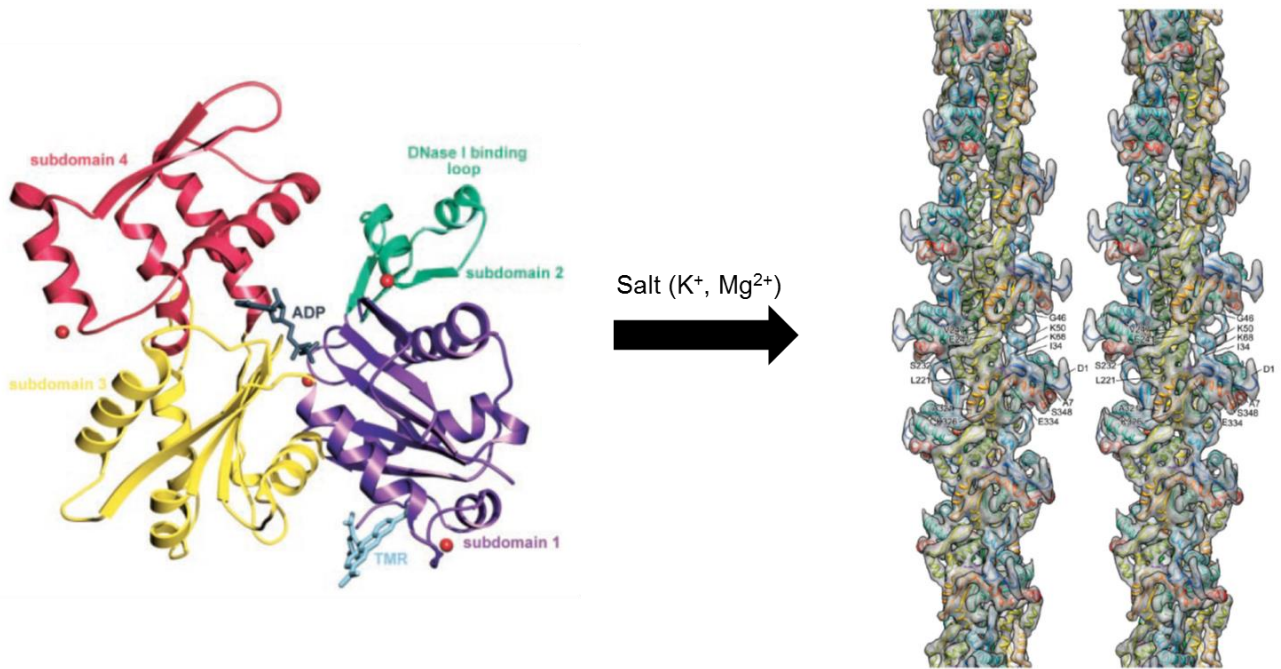


Figure 1. **Representation of actin polymerization in presence of salt.** Actin monomer structure depicts four subdomains. Subdomain 1 (purple), subdomain 2 (green) with DNase 1 binding loop, subdomain 3 (yellow) and subdomain 4 (red). Image reference from: (Otterbein, Graceffa, & Dominguez, 2001) (PDB ID: 1J6Z). Namba model of actin filament with fifteen subunits per filament and amino terminus in blue and carboxyl terminus in red. Image from reference: (Fujii et al., 2010) (PDB ID: 3MFP).

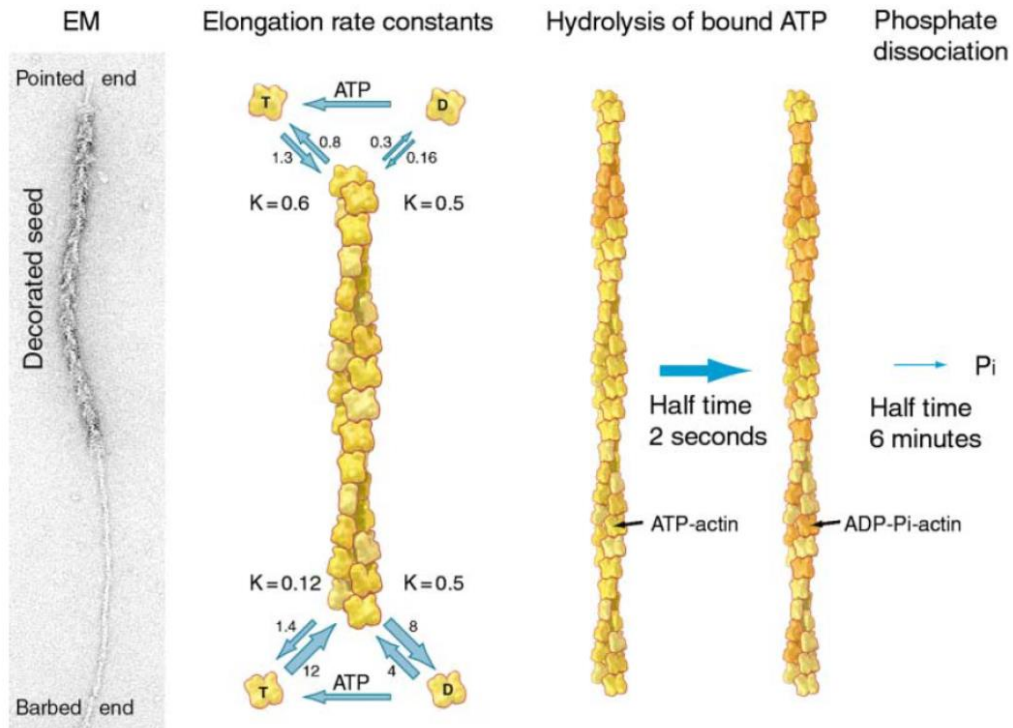


Figure 2. **Elongation of actin filament and ATP hydrolysis with dissociation of phosphate.** The EM image depicts filament seed, and elongation phase of polymerization with ATP-actin. Association ($\mu\text{M}^{-1} \text{s}^{-1}$) and dissociation rate (s^{-1}) constants of monomeric actin. Hydrolysis of ATP bound to actin is fast but release of P_i is slow. Image from reference: (Pollard & Borisy, 2003).

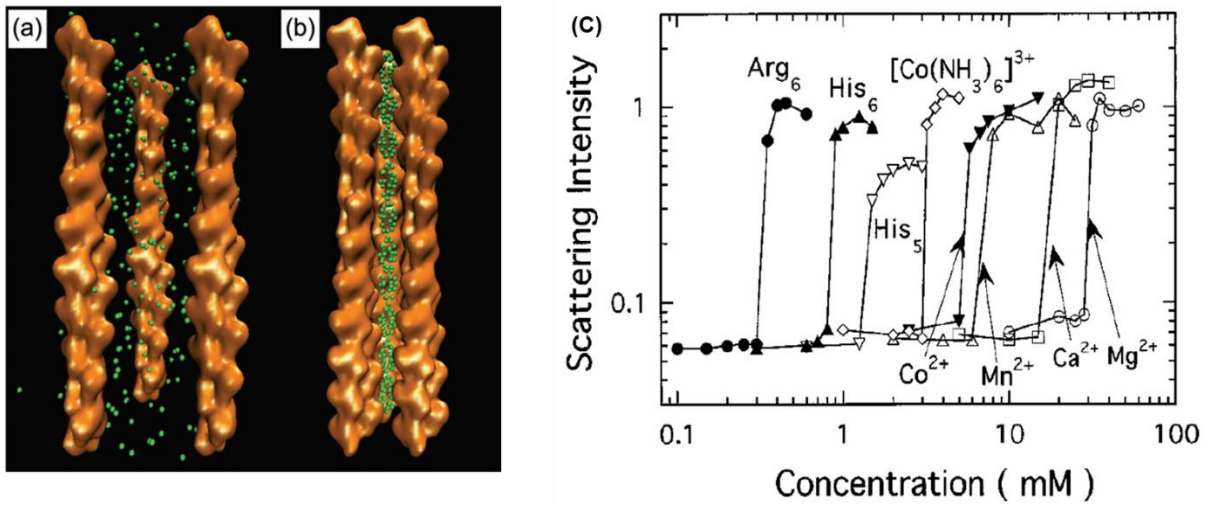


Figure 3. **Schematic representation of actin filament modulation by multivalent counterions.** (A) Uncondensed actin filaments at low multivalent salt concentrations. (B) Condensed filaments at high multivalent salt concentrations that form charge density wave (CDW) and assembly into a bundled structure. Image from reference: (Angelini et al., 2005). (C) Light scattering of F-actin in various divalent salts, results show threshold for bundle formation. Image from reference: (Tang & Janmey, 1996).

CHAPTER TWO: MATERIALS AND METHODS

2.1 Protein and Sample Preparations

Actin was isolated from rabbit skeletal muscle acetone powder, gel filtered over Sephacryl S-300 equilibrated in buffer A (0.2mM CaCl₂, 1mM NaN₃, 2mM Tris-HCl pH 8.0, 0.2mM ATP, 0.5mM DTT) as described (Kang et al., 2012). Rhodamine labeled rabbit muscle actin (>99% purity) was purchased from Cytoskeleton, Inc. (Denver, CO). 50μL of buffer A was added to Rhodamine labeled G-actin to make the concentration 0.4mg/ml. Calcium bound G-actin was then subject to cation exchange of Ca²⁺ to Mg²⁺, 20mM EGTA and 1mM MgCl₂, equal to the initial concentration of G-actin plus 10μM was used to convert the calcium bound G-actin to magnesium bound G-actin (De La Cruz et al., 2000; Kang et al., 2012). Polymerization occurred by the addition of 0.1 volume of 10X polymerization buffers (10-40mM Ca²⁺ and Mg²⁺, 10mM Imidazole pH 7.0, 1mM ATP and 1mM DTT) in separate and varying monovalent and divalent salt concentrations.

2.2 Sedimentation Assay

To quantify the percentage of bundles at varying cation concentrations, low-speed sedimentation assay was performed at 15,000 rpm for 40 minutes at 4°C. The centrifuge used was Sorvall _MTX 150 (Thermo Fisher Scientific) and rotor was s100-AT3-2029 (Thermo Fisher Scientific). A total of 100μL of actin sample was placed into each centrifuge tube. The concentration of actin would be 10 μM for all varying salt conditions. After centrifugation, the supernatant was removed and placed into corresponding Eppendorf tubes (McCullough et al., 2011; Takatsuki et al., 2014). The remaining pellet was re-suspended with 30μL of the equivalent polymerization buffer condition, and then placed in separate Eppendorf tubes. To check for actin

in the solutions a standard SDS-PAGE gel electrophoresis was performed, molecular weight marker Bio-Rad (Cat: 64076918) with 12% Bis-Tris gel. Wells labeled as alternating supernatant and pellet conditions to differentiate the samples (Takatsuki et al., 2014).

2.3 TIRF Microscopy Imaging

Actin bundles were immobilized on microscope slides by poly-L-lysine (Sigma-Aldrich, St. Louis, MO, USA). Images of actin bundles were taken using a Nikon Eclipse Ti TIRF microscope equipped with a Hamamatsu Image EM X2 CCD camera, a 100X oil immersion objective and Nikon LU-N4 laser with wavelengths 405-640nm to achieve total internal reflection. Nikon imaging software was used to image the actin bundles and perform analysis. Imaging was performed at room temperature (~ 22 °C) (Kang et al., 2012). Microscope slides were cleaned by absolute ethanol, sonication bath and then extensive rinsing with ddH₂O as described (Kang et al., 2014).

2.4 Actin Bundle Persistence Length (L_p) and Average Length Analysis

Actin bundle analysis was performed using ImageJ, *Persistence* (Graham et al., 2014) and Origin softwares. Images were uploaded into ImageJ then subjected to enhancement as described (Graham et al., 2014; Kang et al., 2014; Kang et al., 2012). The augmentation of the images included background subtraction, smoothing, contrast enhancement, thresholding and skeletonization. The size of the pixel in microns is determined from the TIRF microscope. In this study the size of pixel was set to be 0.16 $\mu\text{m}/\text{pixel}$. Averaged bundle length was determined by population mean through *Persistence* (Graham et al., 2014) and analyzed with Origin. The L_p values were analyzed from angular correlation data of bundles (>25 images $n=100-300$ bundles) as described (Graham et al., 2014; Kang et al., 2012; McCullough et al., 2011).

Bending persistence lengths (L_p) of actin bundles were determined by Equation (1) from the two-dimensional average angular correlation ($\langle C_s \rangle$) of the tangent angles (θ) which goes along the segment length of the filament (s) (Crevenna et al., 2015; Graham et al., 2014; Kang et al., 2012; McCullough et al., 2011):

$$\langle C(s) \rangle = \langle \cos[\theta(s) - \theta(0)] \rangle = e^{-s/2L_p} \quad (1)$$

The polymer bending rigidity of the bundle can be defined by using Equation (2) in which L_p is the persistence length, κ is the flexural rigidity of the bundle and $k_B T$ using Boltzmann's constant to signify the thermal stability of the bundle (Graham et al., 2014).

$$L_p = \frac{\kappa}{k_B T} \quad (2)$$

2.5 TEM Imaging and Bundle Thickness Analysis

5 μ L of sample solution was loaded onto an EM-grid with continuous carbon film that was rendered hydrophilic by glow discharge. After 60sec sample adsorption, the grid was washed 3 times using droplets of deionized water, followed by negative staining with 5 μ L of 1% uranyl acetate solution. Excess staining solution was blotted using a piece of filter paper. The sample was imaged using Tecnai G2 Spirit TWIN (FEI Co., USA) transmission electron microscope operated at 120kV acceleration voltage. The images were recorded using UltraScan 4000 CCD camera (Gatan Inc., USA). TEM images were used to quantify the diameter of the bundles under the varying salt concentrations. Actin concentrations for imaging was 10 μ M. The pixel diameter (D_p) of each bundle was found using ImageJ length tool, measurement of the scale bar in pixels was determined to indicate nm/pixel (S_p). To calculate the diameter of each bundle analyzed we take (D_p)*(S_p), bundle diameter (B_D) would then be given in nanometers (nm).

2.6 Time-Dependent Bundle Fluorescence Analysis

Fluorescence intensity is a measure of bundle thickness. Imaging of the actin bundles in various time-points were performed using TIRF microscopy. The polymerized bundle samples were placed on microscope coverslips coated with poly-L-lysine (Sigma-Aldrich, St. Louis, MO, USA). Nikon imaging software allowed for analysis of bundle fluorescence. The diameter was measured by length analysis of each individual bundle sample, number (n) of bundles measured = 4800. Length tool was placed along the cross section of each individual bundle. Fluorescence analysis of the data was recorded in μm from samples in steady state bundle imaging experiments.

2.7 Dynamic Light Scattering (DLS)

Analysis of all actin bundle samples solutions were performed using a Zetasizer Nano ZS90 DLS system equipped with a green laser (532 nm, 4 mW) and an avalanche photodiode detector (APD) (quantum efficiency >50% at 532 nm) (Malvern Instruments Ltd., England)(Zheng, Cherubin, Cilenti, Teter, & Huo, 2016). All measured light scattering intensities are displayed as a photon count rate with a unit of kilo count per second (kcps). A Hellma cuvette QS 3 mm was used as sample container. The Malvern DTS 5.10 software was applied to process and analyze the data. All measurements were conducted at a maximum laser power of 4 mW. For each sample solution, two DLS measurements were performed with a fixed run time of 10sec. The scattering angle was set at 90° (Zheng et al., 2016).

A 50 μL of as-prepared actin monomer solution with the actin concentration set to 1mg/ml at 24 μM and diluted to 10 μM , was first mixed with 5 μL 0.1 volume of 10X polymerization buffers separately in a 1.5 mL microcentrifuge tube, followed by quickly transferring into the Hellma cell

for measurement. To prevent aggregation of bundles in the cuvette, slight agitation of the solution was performed by minimal disturbance 10sec before the proceeding time-point. DLS analysis was kinetically conducted every 10min in a total 2-hour time frame. The measurement results were directly reported as scattered light intensity.

2.8 Molecular Dynamics Simulation

The simulated structure of the actin bundle was subjected to a molecular dynamics (MD) simulation using NAMD (Phillips et al., 2005), and consisted of two actin filaments, with 4 monomers per filament. The monomers in the first filament are labeled by P1, P2, P3, and P4, and the monomers in the second filament are labeled by P5, P6, P7, and P8. To construct the actin bundle model, we duplicated the Namba model of a single filament (Fujii et al., 2010) (PDB ID 3MFP) and shifted the two filaments by 30 Å. The built all-atom model of the actin bundle was solvated in a 135 Å x 200 Å x 200 Å box of TIP3P water (Jorgensen, Chandrasekhar, Madura, Impey, & Klein, 1983). The system (with the total electrostatic charge of -96 elementary units) was ionized by adding 48 divalent ions. Two systems were prepared: one with Ca²⁺ and one with Mg²⁺ ions. The initial placement of the ions was accomplished with MEAD (Bashford, 1997). A 12 Å minimum distance between the ions prevented the ionic clusterization near the potential binding sites. The final structure included 472,695 atoms. The simulation analysis was performed by VMD (Humphrey, Dalke, & Schulten, 1996).

The simulations employed CHARMM26 + CMAP force field (MacKerell, Feig, & Brooks, 2004) and were performed in the NPT regime (the constant temperature of 25°C and the constant pressure of 1 atm). The simulations used periodic boundary conditions and the Particle Mesh Ewald method (Darden, York, & Pedersen, 1993) for full electrostatic calculations, and a

multiple time-stepping scheme with a 2fs basic time-step. The simulation protocol included 25,000 steps of steepest-descent minimization followed by a 2ns equilibration and a 20ns production run. The coordinates of the atoms of the system were saved every 2ps, resulting in an MD trajectory of 10,000 frames.

CHAPTER THREE: RESULTS

3.1 Divalent Cations Modulate Bundle Mechanics and Size Distribution

The bending stiffness of cation-induced actin bundles was determined from persistence length (L_p) analysis of TIRF microscopy images (Figure. 4A and 4B). Estimation of bending stiffness was conducted utilizing the exponential fits in relation to the average cosine correlation function from Equation (1) (Supplemental Figure. 1). Low-speed sedimentation assay was conducted to evaluate bundle formation in each salt condition (Supplemental Figure. 2A and B). The analysis revealed bundle percentages were comparable throughout the divalent cation concentrations (Supplemental Figure. 2C). Neither potassium or sodium ions induce bundles at the range of concentrations (100-300mM), consistent with a previous study showing optimal monovalent salt requires >1M concentrations for bundle formation (Yu & Carlsson, 2003) (Supplemental Figure. 3). Ca^{2+} - and Mg^{2+} -induced bundles have similar stiffness from 10mM to 30mM salt concentrations (Figure. 4B). 40mM Ca^{2+} displays potential saturation limit as a decrease in L_p is observed. However, once the divalent concentrations rise to 40mM there is a deviation in the L_p between the actin bundles. The difference between the bending stiffness stems from potential instability in relation to high concentrations of Ca^{2+} present within the filaments. On the other hand, Mg^{2+} bundles represent enhanced stability and stiffness.

Ionic short range interactions affect steady-state average bundle lengths as well as length distributions. The average length peaks at 20mM for both divalent cations, and increasing salt concentrations produce shorter bundles (Figure. 4C). More importantly, both divalent cations lead to a narrowing of the bundle length distribution (Figure. 4D and E). The main form of growth for actin bundles is indicated with end to end longitudinal aggregation at high salt concentrations, in

which these bundles have a finite size (Lai et al., 2007). Growth of bundles is achieved in phases which begin with rapid lateral growth, followed by longitudinal growth (Lai et al., 2007).

3.2 Divalent Cations Modulate Bundle Thickness

Analysis of TEM images determined bundle thickness dependent on divalent cation concentrations. Images display polymerization of actin filaments occurring throughout each salt condition (Figure. 5 A-F). Diameter of bundles correlate to increase in cation concentrations with low Ca^{2+} and Mg^{2+} salt forming bundles but are structurally disorganized. 20mM Ca^{2+} and Mg^{2+} concentrations indicate polymerization is occurring, and the bundles have begun to form into parallel organized structures. High salt concentrations of both Ca^{2+} and Mg^{2+} display bundle diameter enhancement along with organization of filaments into ordered parallel assemblies. Bundle diameter is reduced in the lower salt concentrations indicating fewer filaments aggregating to form bundles (Figure. 5G). The variation in diameter is dependent on salt concentration for both divalent cations. At high salt conditions bundles of large diameter are produced, indicating finite bundle thickness and minimum energy configuration packaging to reduce binding energy as the bundle is formed (Haviv, Gov, Ideses, & Bernheim-Groswasser, 2008). In addition, varying divalent cation concentrations lead to a broadening of bundle diameter distributions (Supplemental Figure. 4).

3.3 Visualization of Time-Dependent Bundle Formation

To directly monitor the cation mediated bundling process, we conducted TIRF microscopy imaging in real time (Supplemental Figure. 5). The average bundle lengths were analyzed to determine cation effect on assembly dynamics (Figure. 6A and B). While both divalent cation induced bundles reach a steady state of elongation, growth of Mg^{2+} induced

bundles exhibit rapid growth and sharp decrease in bundle length over time. The 30mM Mg^{2+} displays the most prominent elongation phase, indicating swift bundle development and organization. In contrast, Ca^{2+} bundles demonstrate steadied growth and reach a stable bundle length over time. However, the 30mM Ca^{2+} has shown to decrease in length indicating a limitation in growth potential. In accordance to the results obtained, a correlation between average bundle length and DLS measurements (Figure. 7) can be visualized.

Time-dependent fluorescence intensities of bundles was measured to evaluate how bundle thickness fluctuates in varying concentrations. Increasing cation concentration correlates to enhanced fluorescence as seen in Figure. 6C and D. In regards to the lower divalent cation concentrations, fluorescence intensities point towards small bundle diameters over time. Therefore, bundles below 20mM divalent cations are less organized and display a reduced filament packing density. The 30mM divalent concentrations indicate the greatest bundle thickness with Mg^{2+} having the highest fluorescence intensity at the 60min time point. An indication for filaments per bundle, fluorescence intensity allows for an insight into the number of filaments aggregating to form the complex structure under varying cation concentrations. Over time, bundle structure becomes more ordered as cation concentration increases, consistent with TEM imaging analysis (Figure. 5).

3.4 Scattering Intensity Determines Actin Bundle Assembly Dynamics

Dynamic light scattering (DLS) was used to monitor the kinetic process of actin bundle formation (Figure. 7). Filament formation is shown to occupy low cation concentration (10mM) based on their scattering intensity values. When filaments begin to form bundles the scattered light intensity increases to a maximum peak of 3000 kcps. Interestingly, scattering intensity

profiles from DLS analysis correlates well with bundle formation visualized by TIRF microscopy, in particular average bundle lengths. The high variability of the DLS measurements illustrates the dynamic nature of the bundling process. Our results suggest a kinetically favored actin aggregate formation at early stages of bundling. However, over time the bundle assembly reaches a thermodynamically stable state as demonstrated by scattered intensity profiles.

Supplemental Figure. 6 demonstrates scattered intensities of 20mM Ca^{2+} and Mg^{2+} with an actin concentration of 5 μM . The lower concentration was chosen to understand the behavior of bundle assembly in varying divalent cations when there is limited actin concentration. We observed cyclic scattering with k_{cps} values ranging from 200-800. In contrast to the results obtained in Figure. 7, there was no steady state reached during the experimental time-frame with the 5 μM samples. This behavior could potentially be due to thermodynamic movements of actin in solution affecting DLS measurements. Based on the identical scattered intensity fluctuations, Ca^{2+} and Mg^{2+} appear to have similar physical properties when polymerized with equal cation concentrations (Scharf & Newman, 1995).

3.5 Specific Cation Binding Modulates Actin Bundle Formation

The molecular dynamics simulation was utilized to investigate cation interactions between filaments. Four monomers were used for each filament, and the filament was duplicated and translated 30 \AA , the displacement and angles of the monomers are labeled P1, P2, P3, P4, P5, P6, P7, and P8 (Figure. 8A). In filament 1, monomer P1 displaced 22 \AA and rotated 40 $^\circ$, monomer P2 displaced 7 \AA and rotated 25 $^\circ$, monomer P3 2 \AA and rotated 5 $^\circ$, and P4 displaced around 20 \AA and rotated 20 $^\circ$ from their initial positions. In filament 2, monomer P5 displaced 15 \AA and rotated 20 $^\circ$, monomer P6 displaced 1 \AA and rotated 12 $^\circ$, monomer P7 4 \AA and rotated

20°, and P8 displaced around 7Å and rotated 15° from their initial positions (Figure. 8B). The monomers P1 in filament 1 and monomer P5 in filament 2 are adjacent to each, moreover they move about 10Å toward each other. P1 and P6 at some point of the simulation are forced away from each other, but return to their initial positions. Monomer P1 and P7 move 20Å closer by the end of the simulation. The distal monomers in each filament (P1 and P8) remain constantly distanced from other. Monomer P2 from filament 1 during the simulation starts approaching P5 and P6 from filament 2, but at the end of the simulation returns close to its initial coordinates. Distance of P2 from monomers P7 and P8 remains constant during the simulation. Monomer P3 remains at a constant distance from P5, P6, P7 and P8 during all of the simulations. Finally, P4 moves about 10Å closer to P6 and maintains a constant distance from P5, P7, and P8 from filament two. Herein, we analyzed the minimum distance and the average distance of the filaments (Figure. 8C).

Our simulations suggest negatively charged amino acid residues interact with specific cation binding sites when forming bundles. The main interactions and bundling sites are located between subdomains 2 and 4 (Figure. 9). ASP 51 and 363 along with GLU 51 are consistently binding with Mg²⁺ ions, but the steric effects determine how efficient the cation binding is between the filaments. In addition, a cluster of aspartic acid residues from both filaments can be observed to interact with Mg²⁺ ions. Helical twisting motion in the distal monomers are visualized for both filaments. Grason et al. (Grason & Bruinsma, 2007) proposed a hexagonal rod model suggesting filaments twist as the bundle is formed. This theory is supported by previous experimental studies that have found evidence of symmetry breaking (twisting) in the actin filaments, which results in sections with larger charge distributions (Angelini et al., 2003).

This twisting is proposed to allow the filaments to electrostatically accommodate themselves to the most thermodynamically stable conformation.

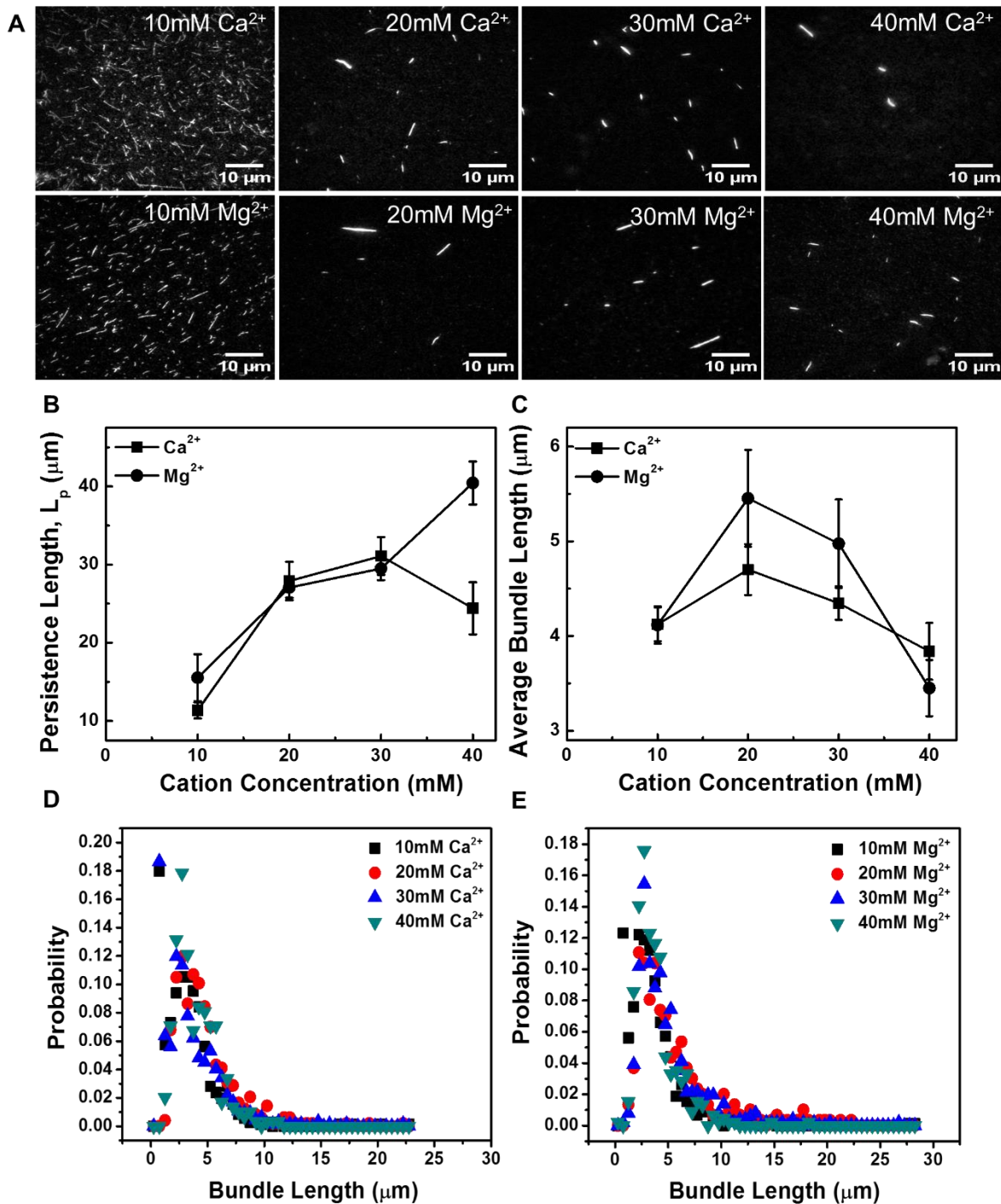


Figure 4. **Cation induced polymerization affects actin bundle mechanics.** (A) Representative TIRF microscopy images of bundles formed by divalent cations, Ca^{2+} (top) and Mg^{2+} (bottom). Buffers: $\text{CaI}_{7.0}$ and $\text{MgI}_{7.0}$ (10mM Imidazole pH 7.0 with varying $[\text{Ca}^{2+}]$ and $[\text{Mg}^{2+}]$, 1mM ATP and 1mM DTT). Actin concentration for imaging is 8 μM . (Scale bars, 10 μm). (B) Persistence length analysis of actin bundles display similar stiffness up to 30mM divalent salt. (C) Average bundle length decreases in response to rise in cation concentration. (D-E) Distribution of bundle length over varying divalent concentrations. Uncertainty bars represent the standard error (SE).

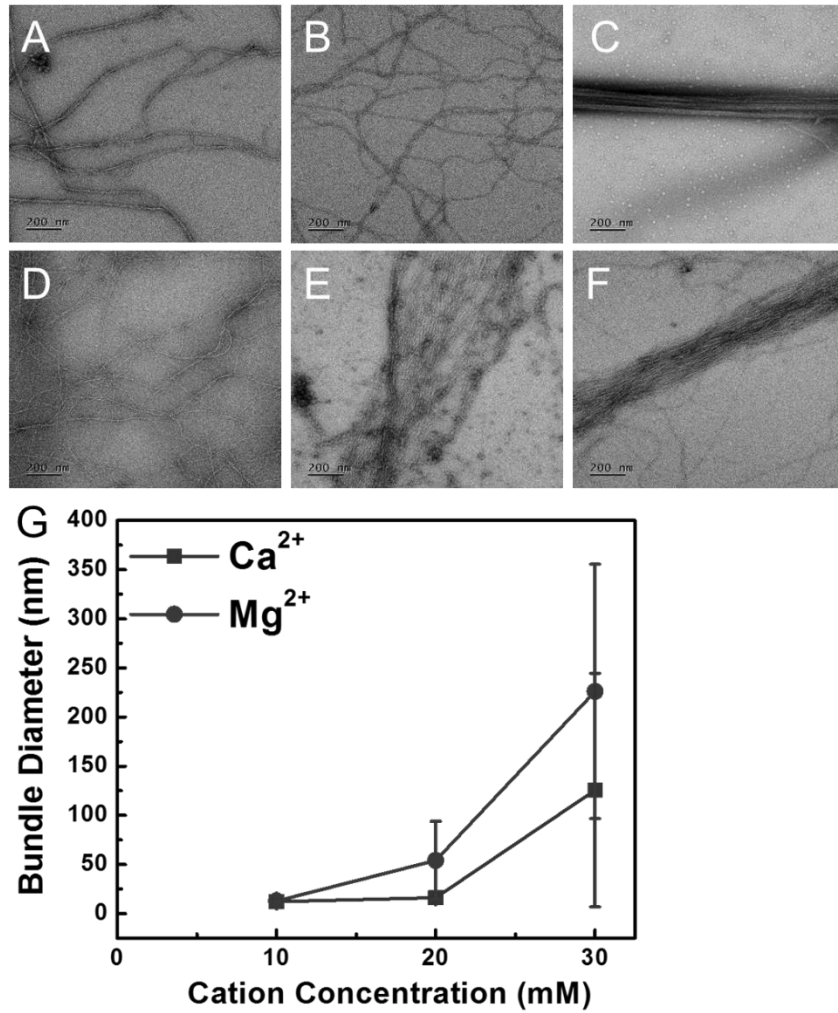


Figure 5. **TEM imaging displays modulation of bundles by divalent cations.** Representative TEM images of actin bundles demonstrate progression of actin filaments into ordered parallel structures with increase in cation concentration. Polymerization buffers: CaI_{7.0} and MI_{7.0}, 10mM Imidazole pH 7.0, 1mM ATP and 1mM DTT. (A-C) Ca²⁺ and (D-F) Mg²⁺ actin bundles. Actin concentration is 10 μ M. (Scale bars, 200nm). (G) Analysis of bundle thickness illustrates growth in diameter as result of increase in divalent concentrations. Uncertainty bars represent the SE.

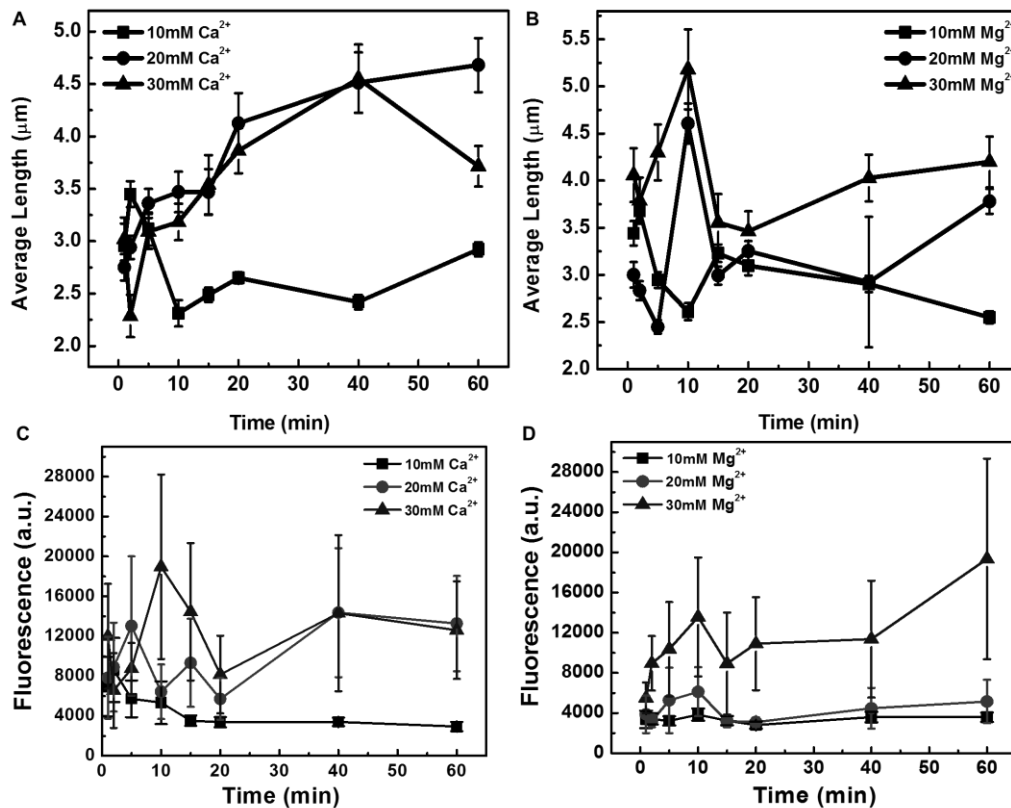


Figure 6. **Time-dependent average length and fluorescence of bundles.** Bundle formation was induced with $10\mu\text{M}$ actin in polymerization buffer ($\text{CaI}_{7.0}$ and $\text{MI}_{7.0}$, 10mM Imidazole pH 7.0, 1mM ATP and 1mM DTT) containing varying divalent cation concentrations. TIRF microscopy images (Supplemental Figure. 3) of bundles at each time point were analyzed ($N= 100$ bundles per condition). (A-B) Average length indicates dynamic bundling process over time, (A) Ca^{2+} and (B) Mg^{2+} induced bundle. (C-D) Fluorescence intensity correlates bundle thickness, (C) Ca^{2+} and (D) Mg^{2+} . Uncertainty bars represent the SE.

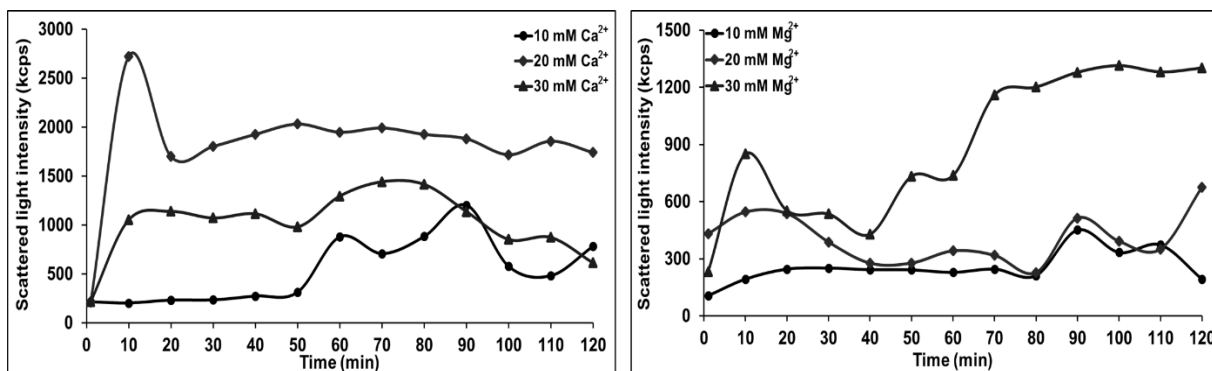


Figure 7. **DLS indicates kinetic and thermodynamic polymerization of actin bundles.** High variability illustrates dynamic nature of bundling process. Over time bundle assembly reaches thermodynamic steady state. Scattering intensity represents bundle formation in kilo count per second (kcps). Experiment performed over 2-hour time frame with 10min interval readings. Measurements were performed at interval readings of 10sec. Actin concentration is 10 μ M per sample condition.

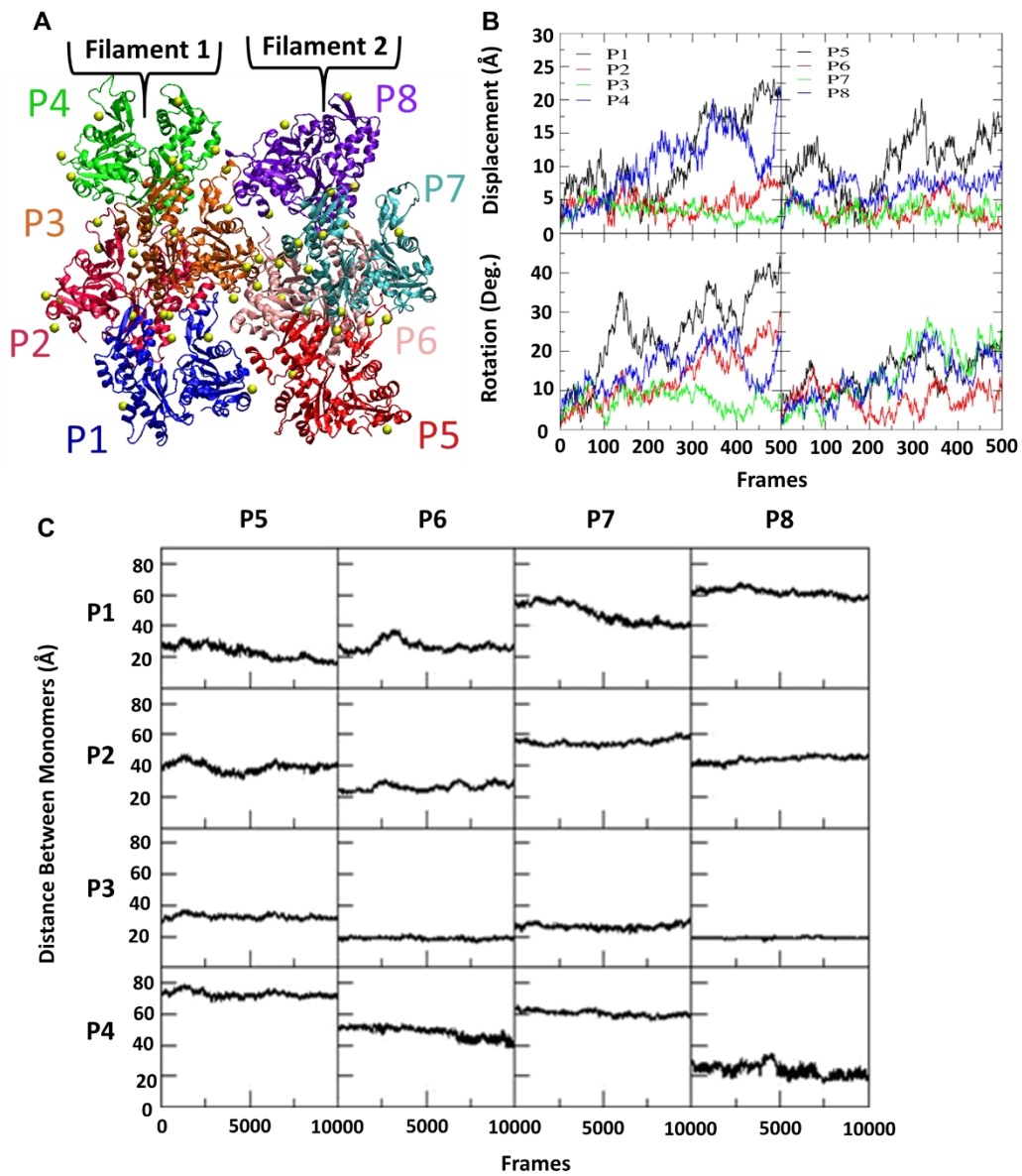


Figure 8. **Structural dynamics of simulated actin bundle.** (A) Namba model for MD simulation indicates interactions occurring at P1-P4 and P5-P8. (B) Displacement and rotation of individual monomers during simulation. (C) Evolution of the monomer-monomer distance for each pair of interactions during the simulation.

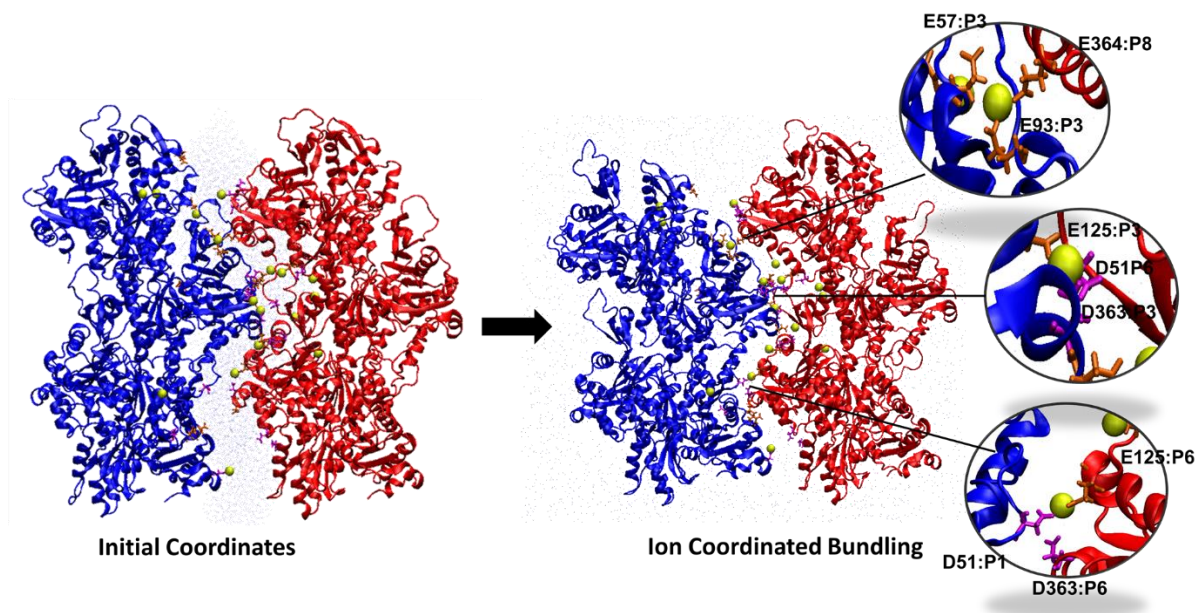


Figure 9. **Cations and actin subdomain interactions form bundles.** Simulation reveals the electrostatic interaction between actin filament (PDB ID: 3MFP) subunits. Comparison of the bundle structure before and after the simulation reveals the ion-induced bundling in three main positions. Filament and Mg²⁺ interaction with amino acid residues aspartic acid (D) and glutamic acid (E).

CHAPTER FOUR: DISCUSSION

The effect of cations on bundle structure can be attributed to ionic radius, charge density and site specific interactions. Ionic radius contributes to properties of metal ions such as bond energy and polarizability (Carafoli, 1987; Feig & Uhlenbeck, 1999; Koculi, Hyeon, Thirumalai, & Woodson, 2007). Preceding research has demonstrated the importance of Mg^{2+} condensation and RNA stability, the small ion is capable of strong metal-oxygen bonds and displays a reduction in its polarizability (Koculi et al., 2007). In comparison to Ca^{2+} , Mg^{2+} produces a higher charge density and stable RNA folding. Meanwhile, although slightly lower in charge density, Ca^{2+} produces dynamic and broader RNA folded structures (Koculi et al., 2007). Based on our results, we propose ionic radius influences ion and protein interactions, therefore facilitating ion protein binding constraints (Carafoli, 1987), packing density and mechanical modulations. Charge density waves are formed by counterion interactions orientated parallel to the actin filaments (Angelini et al., 2003). Because of the CDW, mechanical fluctuations in symmetry can be observed, over-twisting the filaments to an energy stable conformation (Angelini et al., 2003; Claessens et al., 2008). Our results correlate over-twisting to promote enhanced bundle stiffness and assembly, evident in the increase of bundle packing density and L_p measurements.

Discrete binding sites can impact filament assembly, disassembly and structural mechanics associated to binding of cations and ABPs. Site specific substitution elucidated the dependence of salt interactions with charged amino acid residues on actin monomers (Kang et al., 2012). Structural bioinformatics predicated the existence of two separate binding sites termed “polymerization” and “stiffness” (Kang et al., 2014; Kang et al., 2012). In addition, the “stiffness” site is located at the junction of DB-loop and subdomain 3, therefore, mutation of this precise

location has shown its importance to filament mechanics and structural integrity (Kang et al., 2012). Specific cation binding sites have been determined to promote actin filament polymerization and enhance filament stiffness (Kang et al., 2012). Research on cofilin (Kang et al., 2014) has already demonstrated interactions between the stiffness cation and cofilin binding sites. The overlap between the severing protein and the cation site promote ion release, therefore the filament becomes flexible. The interaction demonstrates mechanical modulation associated to cation binding on precise locations. We propose, a distinct “bundling” site on the outer residues which would affect inter-filament mechanics and promote bundling when ions occupy these specific positions.

Persistence length is characterized by flexural rigidity of a polymer such that bundle bending stiffness depends largely on the number of filaments, as well as cross-linker effectiveness (Bathe et al., 2008; Claessens et al., 2006). Research has established that ABP induced bundles have high persistence lengths dependent on actin:ABP ratios. (Bathe et al., 2008; Claessens et al., 2006; Takatsuki et al., 2014) Moreover, fascin has demonstrated tightly packed, ordered helical twisting of actin bundles as a result of more effective cross-linking (Claessens et al., 2008). Therefore, by increasing fascin:actin ratios, a significant rise in L_p occurs, with 1:2 ratio having the highest bundle stiffness (Takatsuki et al., 2014). However, fascin bundling is limited by the protein concentration, as well as the number of binding sites (Breitsprecher et al., 2011; Claessens et al., 2008; Jansen et al., 2011). In comparison to our results, when cation-induced bundle flexural rigidity was calculated and compared to that of fascin, the ABP was significantly more adept at enhancing stiffness with a relatively small amount of filaments (Claessens et al., 2006). However, the evidence we present illustrates divalent bundle density to contain a greater number of filaments than fascin can bundle with enhanced efficiency. Although, the binding protein is an effective

cross-linker it has been shown to improve severing capabilities of cofilin while readily assembling and disassembling bundles *in vitro* (Breitsprecher et al., 2011). We propose the bundles induced by divalent cations are potentially more resistant to shear stress and external forces, due to the number of filaments densely packed and the overall electrostatic attraction between the filaments.

In accordance to the results obtained, the highest concentrations of cations most efficiently reduced bundle length. As the bundles grow, additional cations become condensed in between filaments allowing for the charge of the bundle to remain constant (Henle & Pincus, 2005). Steric interactions prevent internal bundle ion density from surpassing the packing density, and resulting in bundle size increasing by short range electrostatic repulsion (Henle & Pincus, 2005). Size and shape of the cations have the strong ability to influence condensation of the bundles and thereby affect the rate of bundle formation (Wong & Pollack, 2010). If high cation conditions are permitting filaments to condense at an enhanced rate, then lower concentrations would be presumed to have higher bundle lengths. As the multivalent ion attractive forces become strong enough to induce bundle formation, the entropic and electrostatic resistance to bundle growth becomes weak. Thus, charge density and any resistance towards bundle growth is irrelevant (Henle & Pincus, 2005). Our analysis of steady state and length distributions of bundles indicate variations dependent on cation concentrations, while narrow distributions propose inter-filament electrostatic attractive interactions, in which protein cross-linking is not necessary (Biron, Moses, Borukhov, & Safran, 2005).

Based on our observations, bundle thickness is proportional to cation concentration. Stokes et al. (Stokes & DeRosier, 1991) suggest a two-stage mechanism involving nucleation and growth of bundles. The first, a nucleation phase, is dependent on actin concentration, while the second is

a growth phase dependent on actin binding protein concentrations and time allotted for growth (Jansen et al., 2011; Stokes & DeRosier, 1991). In previous research, filaments aggregated to form a disk-like nucleus, that was later incorporated with fascin to surpass the electrostatic repulsion and overcome thresholds to form bundles (Haviv et al., 2008). Our results indicated a similar disk like process of formation, while also providing evidence of high salt concentration as a mechanism for overcoming effects of electrostatic repulsion. Protein cross-linkers are shown to form bundles with finite width, yet electrostatic attraction can produce finite bundle diameter by either short range interactions or by attractive energies being suppressed. (Haviv et al., 2008; Henle & Pincus, 2005). Research observations of divalent induced bundle widths correspond to initial rapid lateral growth, followed by longitudinal growth (Lai et al., 2007). Lai et al. (Lai et al., 2007) hypothesized that varying solution conditions could influence bundle order and size. Our EM results validated this hypothesis, indicating increasing salt concentrations do in fact influence bundle organization and diameter.

In contrast to research associated to fascin and α -actinin (Winkelman et al., 2016), our data strongly suggests cation induced bundling results in densely packed bundles and occurs over short filament spacing. It is well established that densely packed bundles are achieved by fascin (Bartles, 2000), while α -actinin promotes widely spaced bundling (Foley & Young, 2014). The average filament distances were shown to be roughly 8nm and 35nm for fascin and α -actinin, respectively (Winkelman et al., 2016). The bundling protein diameters then can influence the packing capabilities of filaments into bundles with diameters of 6nm and 35nm for fascin and α -actinin, respectively (Winkelman et al., 2016). However, in relation to divalent cation rich environments, the filament spacing becomes smaller, falling within the angstrom range and reducing spacing requirements needed to bundle. As a result, the decreased spacing between the

filaments should allow for binding sites to engage more readily with one another across filaments, conceding to increase electrostatic interactions and more efficient modulating of bundle diameter. Thus, distance is a primary factor in bundle formation rather than filament arrangement. Limitations to concentrations and filament spacing for bundling proteins indicate thresholds in assembly, while divalent cations provide the basis for rapid and short range interactive bundling not yet seen with actin binding proteins.

The MD simulations of the actin filament pursued two vital goals. The first goal, was to generate a plausible structure of a multi-filament actin bundle, whereas the second goal sought to provide insight into the effect of divalent cations on both actin bundle structure and its properties. Until now, no experiment has successfully obtained a practical or workable structure of either actin filament or bundle forms, the best approximation being the Namba model refined from electron microscopy measurements (Fujii et al., 2010). Our modeling study aspired to construct a plausible model structure of cation-induced bundling. *In vitro* mutagenesis studies (Kang et al., 2012) showed that multivalent cation binding to actin monomers promoted actin polymerization and further enhanced stiffness specifically at discrete binding sites. Our constructed simulation of a bundle structure was then used to reveal with the highest likelihood the locations of cation binding, especially for those locations situated between filaments and therefore initiate binding, holding the bundled structure (Hocky et al., 2016). Although preliminary, our simulation suggests the existence of specific bundling sites on actin filaments at short distances.

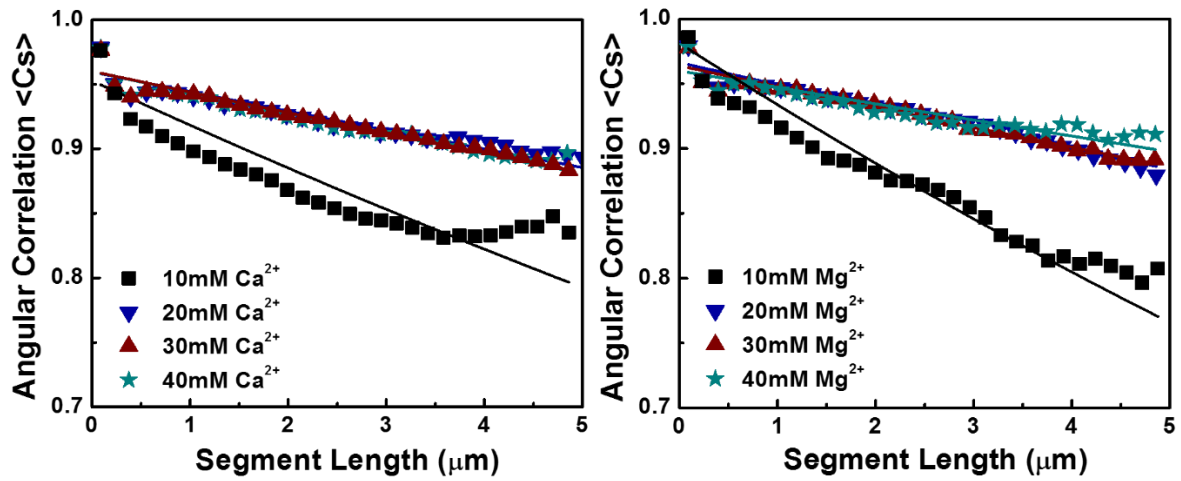
CHAPTER FIVE: CONCLUSION

The fundamental understanding of cation interactions with polyelectrolytes are essential for determining *in vivo* bundling mechanisms. Experimental research on physiological systems such as neuronal growth cones, stereocilia, filopodia, phagocytes and various ABPs will benefit from the results of this study. The most direct implication of this work correlates to elucidating how ABPs, and other ion-dependent mechanisms function under varying concentrations of divalent cations while *in vivo*. Although previous theories proposed have demonstrated the non-specific nature of electrostatic interactions, our study signifies discrete binding locations are detrimental to bundling of actin filaments. *In vivo*, cellular filament density is relatively high compared to what can be achieved by *in vitro* experimentation (Tang & Janmey, 1996). Therefore, continued research is required to provide insight to the consequences of ionic fluctuations in a cell.

The results of this study have shown how environments with high concentrations of ions can modulate the mechanical and structural configurations of the bundle system. Research has since postulated the existence of discrete binding sites and further speculated at the extent of influence it maintains on filament packing into bundled structures. Through this research, properties associated with the actin bundle system have thoroughly been elucidated and have thus shed light on new areas of study that are both exciting and novel with impactful implications. We expect to build upon the foundation of this study for future research with ABPs in varying cation concentrations, ion-induced bundling in crowded environments and exposing the mechanical strength of the actin bundle system utilizing microfluidic devices. These unique and innovative experimental studies would shed light on *in vivo* cellular interactions, which all

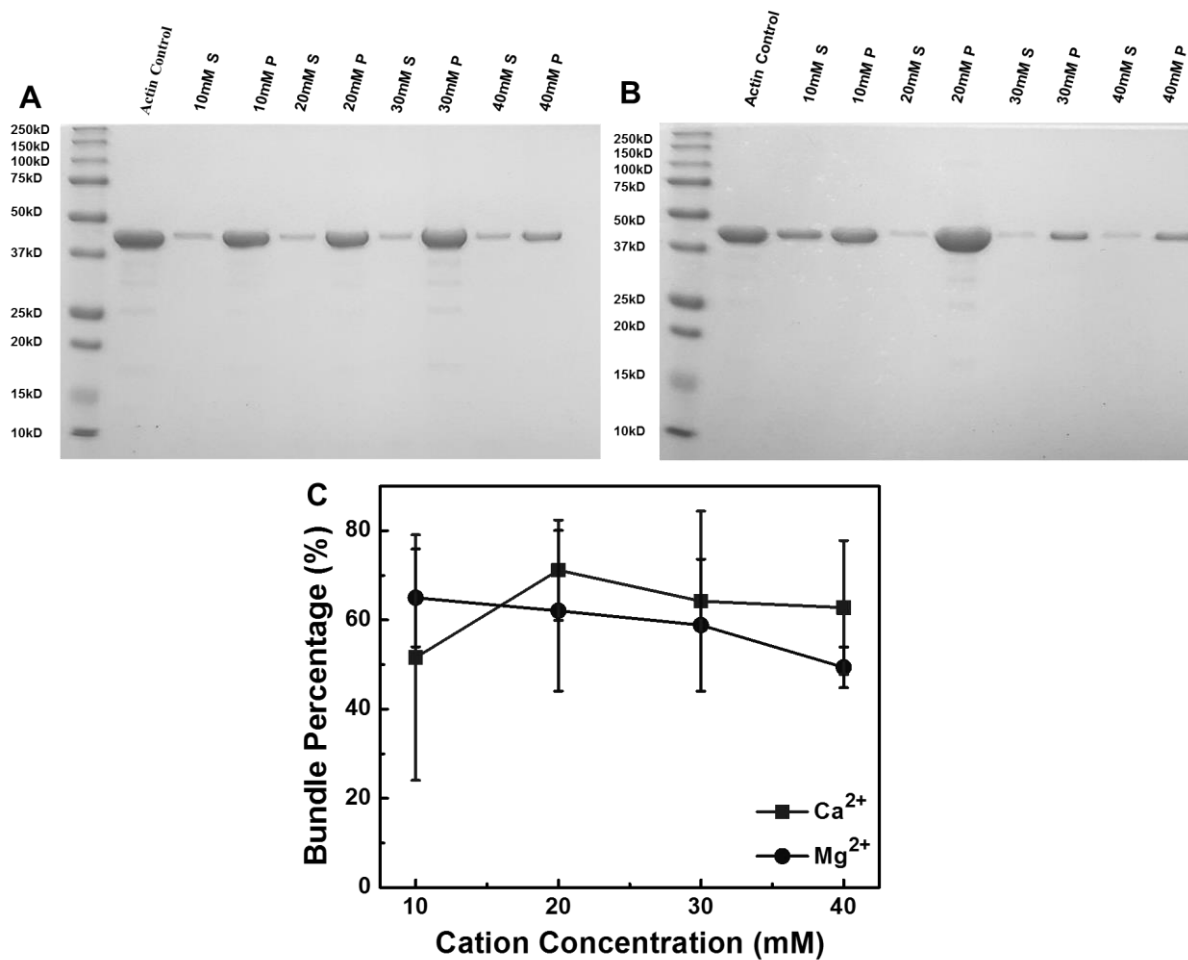
lead back to bundle structure formation. It is my hope that the research performed in this study would provide a foundation for continued experimentation into the understanding of polyelectrolyte bundles and development of *in vivo* applications.

APPENDIX A: DETERMINATION OF ACTIN BUNDLE PERSISTENCE LENGTH



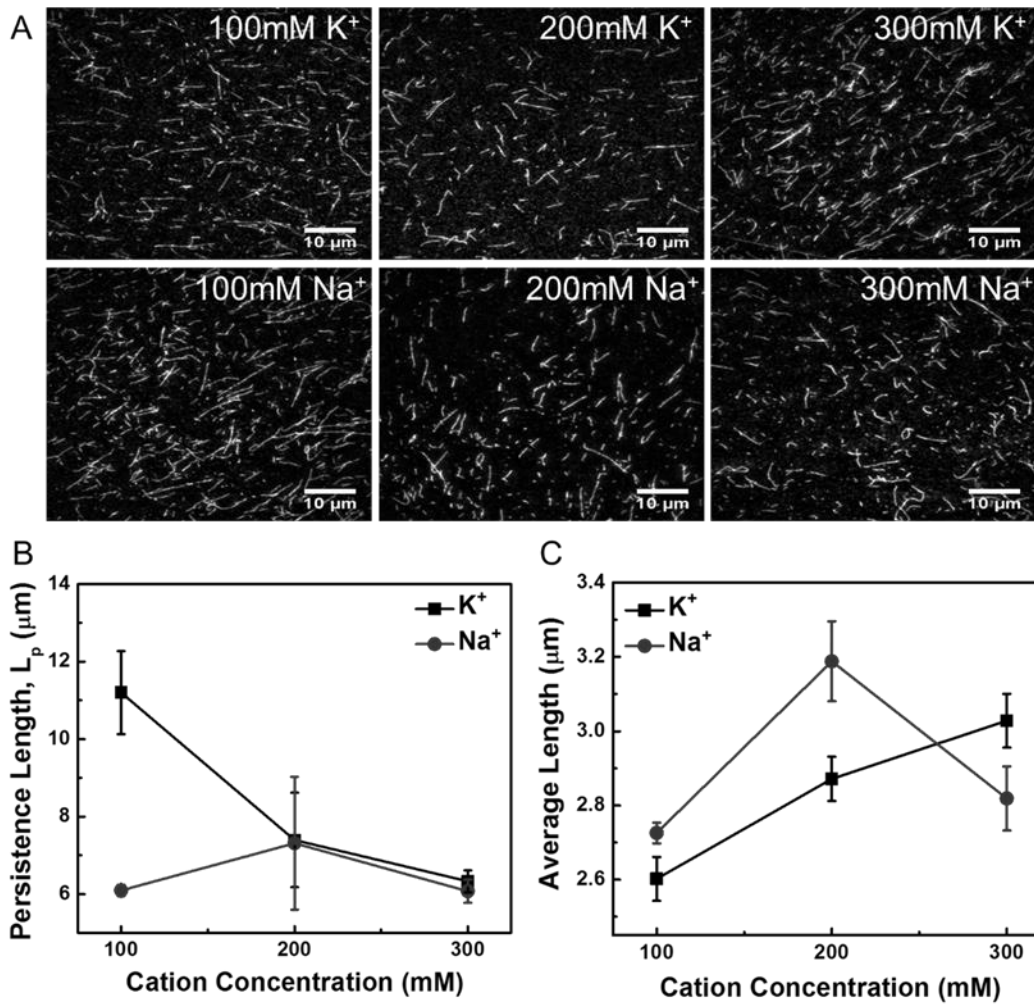
Supplemental Figure 1. The average cosine correlation functions are plotted against bundle segment lengths (s) in accordance to Equation (1). Solid lines illustrate exponential fits obtained using non-linear regression. Analysis was conducted from images collected in Figure. 4A. ($N= 100$ bundles per condition).

**APPENDIX B: LOW-SPEED SEDIMENTATION INDICATES
PERCENTAGE OF BUNDLES PER SALT CONDITION**



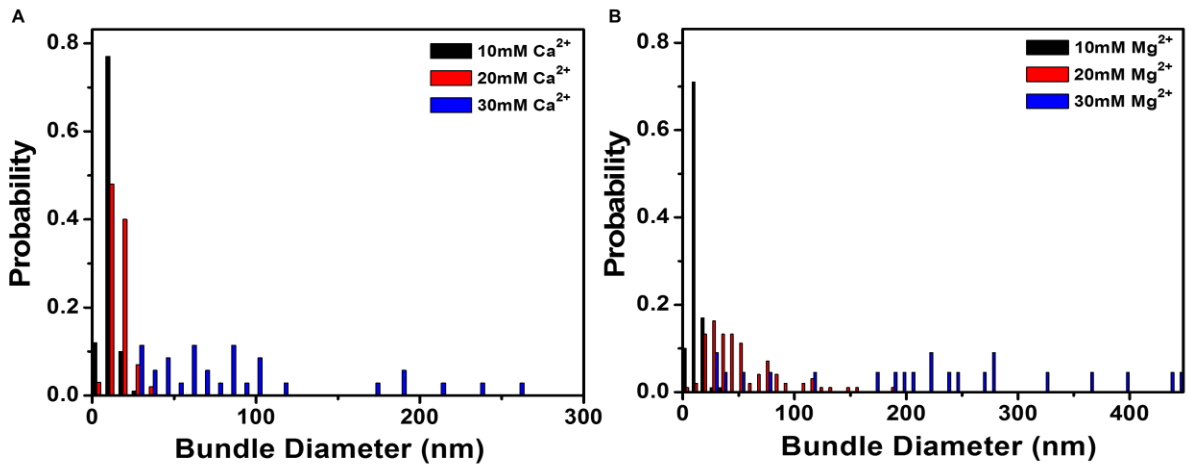
Supplemental Figure 2. Actin bundle samples are shown as alternating supernatant (S) and pellet (P) for each varying salt condition. Bundle polymerization was performed with varying concentrations of buffers: CaI_{7.0} and MI_{7.0} (10mM Imidazole pH 7.0, 1mM ATP and 1mM DTT). Actin concentrations for both (A) Ca²⁺ and (B) Mg²⁺ were 10μM. (C) Analysis of low-speed sedimentation indicates similar bundle percentage as concentrations increase for both divalent cations. Uncertainty bars represent the SE.

APPENDIX C: MONOVALENT CATIONS AFFECT ACTIN FILAMENT ASSEMBLY



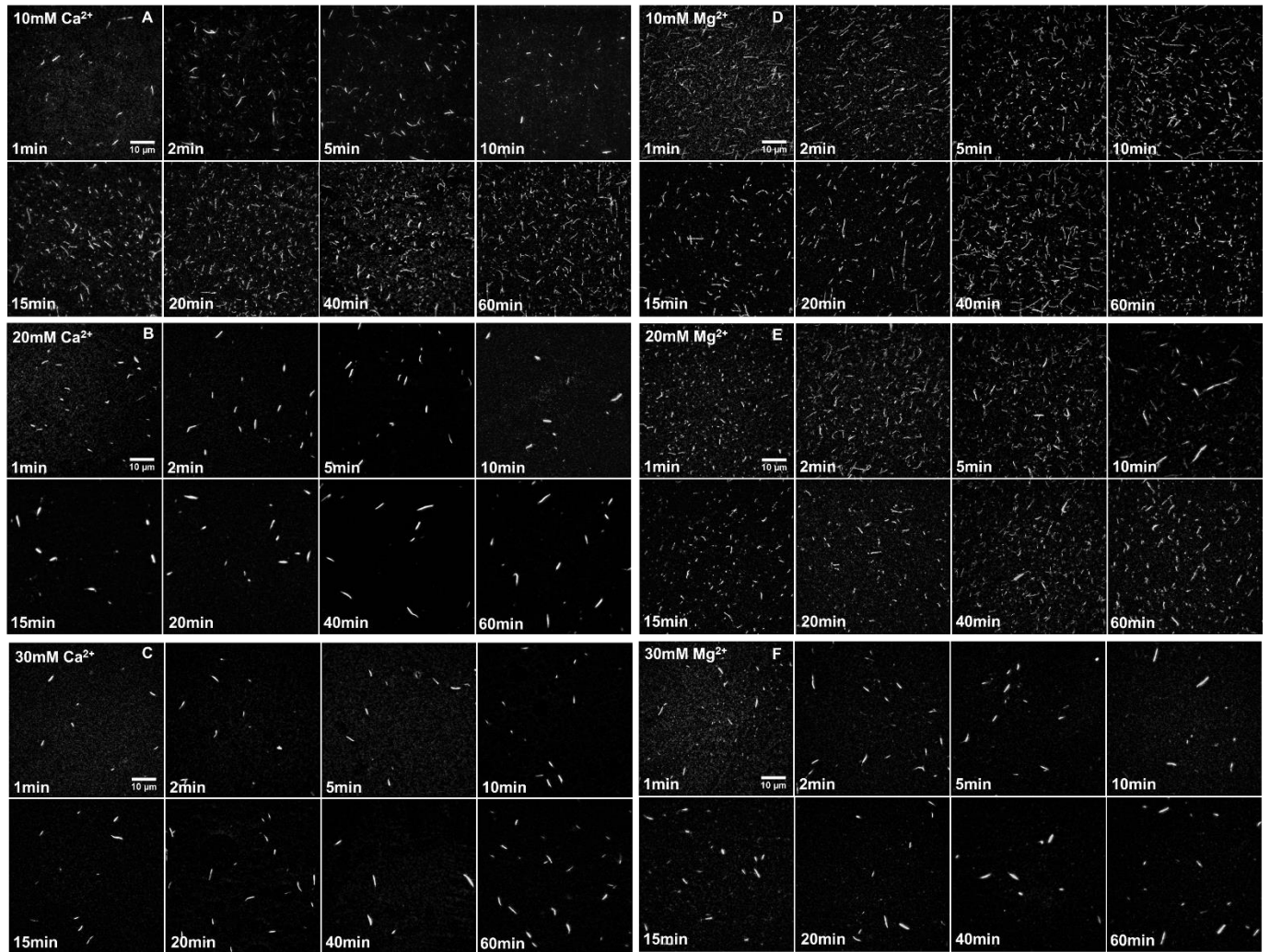
Supplemental Figure 3. TIRF microscopy images of filaments formed by monovalent cations. (A) K^+ and Na^+ . Polymerization of actin filaments were performed with buffers: $\text{KI}_{7.0}$, $\text{NaI}_{7.0}$ (10mM Imidazole pH 7.0 with varying $[\text{K}^+]$ and $[\text{Na}^+]$, 1mM ATP and 1mM DTT). Actin concentration for imaging is 8 μM . (Scale bars, 10 μm). (B) Persistence length (L_p) analysis of monovalent cations on actin mechanics indicate filament stiffness. (C) Average length measurements demonstrate filament polymerization varying in monovalent concentrations. Uncertainty bars represent the SE.

APPENDIX D: DIAMETER ANALYSIS OF TEM IMAGES



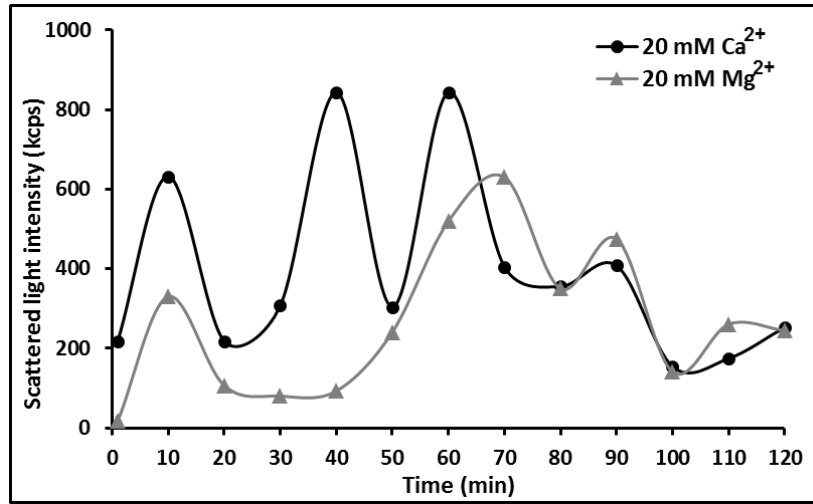
Supplemental Figure 4. Distribution of actin bundle diameters over divalent cation concentrations. (A) Ca²⁺ and (B) Mg²⁺. Polymerization of actin bundles were in buffers: CaI_{7.0} and MI_{7.0} (10mM Imidazole pH 7.0, 1mM ATP and 1mM DTT). Actin concentration is 10μM.

**APPENDIX E: TIME-DEPENDENT IMAGES CORRELATE TO ACTIN
BUNDLE LENGTHS**



Supplemental Figure 5. Representative images demonstrate bundle assembly over time. Actin bundles become ordered structures as divalent concentrations increase. Fluorescence intensity of images illustrates formation of filament aggregates corresponding to cation concentration and potentially indicates filaments per bundle. (A-C) Ca^{2+} and (D-F) Mg^{2+} divalent cations. Buffers: $\text{CaI}_{7.0}$ and $\text{MgI}_{7.0}$ (10mM Imidazole pH 7.0, 1mM ATP and 1mM DTT). Actin concentration is $8\mu\text{M}$. (Scale bars, $10\mu\text{m}$).

APPENDIX F: DYNAMIC BUNDLE FORMATION AT LOW ACTIN CONCENTRATION



Supplemental Figure 6. Light scattering intensity fluctuations are similar in both Ca²⁺ and Mg²⁺. Comparison of the results indicates kinetic and thermodynamic assembly of actin bundles over time. Actin concentration was 5 μ M. Polymerization buffers: 20mM CaI_{7.0} and MI_{7.0}, 10mM Imidazole 7.0, 1mM ATP and 1mM DTT. Measurements were performed at interval readings of 10sec with a total experimental time frame of 2-hours.

REFERENCES

- Angelini, T. E., Liang, H., Wriggers, W., & Wong, G. C. (2003). Like-charge attraction between polyelectrolytes induced by counterion charge density waves. *Proc Natl Acad Sci U S A*, *100*(15), 8634-8637. doi:10.1073/pnas.1533355100
- Angelini, T. E., Sanders, L. K., Liang, H., Wriggers, W., Tang, J. X., & Wong, G. C. (2005). Structure and dynamics of condensed multivalent ions within polyelectrolyte bundles: a combined x-ray diffraction and solid-state NMR study. *J Phys Condens Matter*, *17*(14), S1123.
- Bartles, J. R. (2000). Parallel actin bundles and their multiple actin-bundling proteins. *Curr Opin Cell Biol*, *12*(1), 72-78.
- Bashford, D. (1997). An object-oriented programming suite for electrostatic effects in biological molecules An experience report on the MEAD project. Paper presented at the ISCOPE 97.
- Bathe, M., Heussinger, C., Claessens, M. M., Bausch, A. R., & Frey, E. (2008). Cytoskeletal bundle mechanics. *Biophys J*, *94*(8), 2955-2964. doi:10.1529/biophysj.107.119743
- Biron, D., Moses, E., Borukhov, I., & Safran, S. (2005). Inter-filament attractions narrow the length distribution of actin filaments. *EPL (Europhysics Letters)*, *73*(3), 464.
- Breitsprecher, D., Koestler, S. A., Chizhov, I., Nemethova, M., Mueller, J., Goode, B. L., . . . Faix, J. (2011). Cofilin cooperates with fascin to disassemble filopodial actin filaments. *J Cell Sci*, *124*(Pt 19), 3305-3318. doi:10.1242/jcs.086934
- Carafoli, E. (1987). Intracellular calcium homeostasis. *Annu Rev Biochem*, *56*(1), 395-433.
- Claessens, M. M., Bathe, M., Frey, E., & Bausch, A. R. (2006). Actin-binding proteins sensitively mediate F-actin bundle stiffness. *Nat Mater*, *5*(9), 748-753. doi:10.1038/nmat1718

- Claessens, M. M., Semmrich, C., Ramos, L., & Bausch, A. R. (2008). Helical twist controls the thickness of F-actin bundles. *Proc Natl Acad Sci U S A*, *105*(26), 8819-8822. doi:10.1073/pnas.0711149105
- Crevenna, A. H., Arciniega, M., Dupont, A., Mizuno, N., Kowalska, K., Lange, O. F., . . . Lamb, D. C. (2015). Side-binding proteins modulate actin filament dynamics. *Elife*, *4*. doi:10.7554/eLife.04599
- Darden, T., York, D., & Pedersen, L. (1993). Particle mesh Ewald: An $N \cdot \log(N)$ method for Ewald sums in large systems. *J Chem Phys.*, *98*(12), 10089-10092.
- De La Cruz, E. M., & Gardel, M. L. (2015). Actin Mechanics and Fragmentation. *J Biol Chem*, *290*(28), 17137-17144. doi:10.1074/jbc.R115.636472
- De La Cruz, E. M., Mandinova, A., Steinmetz, M. O., Stoffler, D., Aebi, U., & Pollard, T. D. (2000). Polymerization and structure of nucleotide-free actin filaments. *J Mol Biol*, *295*(3), 517-526. doi:10.1006/jmbi.1999.3390
- De La Cruz, E. M., Roland, J., McCullough, B. R., Blanchoin, L., & Martiel, J. L. (2010). Origin of twist-bend coupling in actin filaments. *Biophys J*, *99*(6), 1852-1860. doi:10.1016/j.bpj.2010.07.009
- Dos Remedios, C., Chhabra, D., Kekic, M., Dedova, I., Tsubakihara, M., Berry, D., & Nosworthy, N. (2003). Actin binding proteins: regulation of cytoskeletal microfilaments. *Physiological reviews*, *83*(2), 433-473.
- Fazli, H., Mohammadinejad, S., & Golestanian, R. (2009). Salt-induced aggregation of stiff polyelectrolytes. *J Phys Condens Matter*, *21*(42), 424111. doi:10.1088/0953-8984/21/42/424111

- Feig, A. L., & Uhlenbeck, O. C. (1999). The role of metal ions in RNA biochemistry. *COLD SPRING HARBOR MONOGRAPH SERIES*, 37, 287-320.
- Fernandez-Valle, C., Gorman, D., Gomez, A. M., & Bunge, M. B. (1997). Actin plays a role in both changes in cell shape and gene-expression associated with Schwann cell myelination. *J Neurosci*, 17(1), 241-250.
- Fletcher, D. A., & Mullins, R. D. (2010). Cell mechanics and the cytoskeleton. *Nature*, 463(7280), 485-492.
- Foley, K. S., & Young, P. W. (2014). The non-muscle functions of actinins: an update. *Biochem J*, 459(1), 1-13. doi:10.1042/bj20131511
- Fujii, T., Iwane, A. H., Yanagida, T., & Namba, K. (2010). Direct visualization of secondary structures of F-actin by electron cryomicroscopy. *Nature*, 467(7316), 724-728. doi:10.1038/nature09372
- Galkin, V. E., Orlova, A., Schroder, G. F., & Egelman, E. H. (2010). Structural polymorphism in F-actin. *Nat Struct Mol Biol*, 17(11), 1318-1323. doi:10.1038/nsmb.1930
- Galkin, V. E., Orlova, A., Vos, M. R., Schroder, G. F., & Egelman, E. H. (2015). Near-atomic resolution for one state of F-actin. *Structure*, 23(1), 173-182. doi:10.1016/j.str.2014.11.006
- Goverman, J., Schick, L. A., & Newman, J. (1996). The bundling of actin with polyethylene glycol 8000 in the presence and absence of gelsolin. *Biophys J*, 71(3), 1485-1492. doi:10.1016/s0006-3495(96)79349-9
- Graham, J. S., McCullough, B. R., Kang, H., Elam, W. A., Cao, W., & De La Cruz, E. M. (2014). Multi-platform compatible software for analysis of polymer bending mechanics. *PLoS One*, 9(4), e94766. doi:10.1371/journal.pone.0094766

- Grason, G. M., & Bruinsma, R. F. (2007). Chirality and equilibrium biopolymer bundles. *Phys Rev Lett*, *99*(9), 098101. doi:10.1103/PhysRevLett.99.098101
- Haviv, L., Gov, N., Ideses, Y., & Bernheim-Groswasser, A. (2008). Thickness distribution of actin bundles in vitro. *Eur Biophys J*, *37*(4), 447-454. doi:10.1007/s00249-007-0236-1
- Henle, M. L., & Pincus, P. A. (2005). Equilibrium bundle size of rodlike polyelectrolytes with counterion-induced attractive interactions. *Phys Rev E Stat Nonlin Soft Matter Phys*, *71*(6 Pt 1), 060801. doi:10.1103/PhysRevE.71.060801
- Hocky, G. M., Baker, J. L., Bradley, M. J., Sinitskiy, A. V., De La Cruz, E. M., & Voth, G. A. (2016). Cations Stiffen Actin Filaments by Adhering a Key Structural Element to Adjacent Subunits. *J Phys Chem B*, *120*(20), 4558-4567. doi:10.1021/acs.jpcc.6b02741
- Howard, J. (2001). *Mechanics of Motor Proteins and the Cytoskeleton*: Mass: Sinauer Associates, Publishers.
- Humphrey, W., Dalke, A., & Schulten, K. (1996). VMD: visual molecular dynamics. *J Mol Graph*, *14*(1), 33-38.
- Jansen, S., Collins, A., Yang, C., Rebowksi, G., Svitkina, T., & Dominguez, R. (2011). Mechanism of actin filament bundling by fascin. *J Biol Chem*, *286*(34), 30087-30096. doi:10.1074/jbc.M111.251439
- Jorgensen, W. L., Chandrasekhar, J., Madura, J. D., Impey, R. W., & Klein, M. L. (1983). Comparison of simple potential functions for simulating liquid water. *J Chem Phys.*, *79*(2), 926-935.

- Kang, H., Bradley, M. J., Cao, W., Zhou, K., Grintsevich, E. E., Michelot, A., . . . De La Cruz, E. M. (2014). Site-specific cation release drives actin filament severing by vertebrate cofilin. *Proc Natl Acad Sci U S A*, *111*(50), 17821-17826. doi:10.1073/pnas.1413397111
- Kang, H., Bradley, M. J., Elam, W. A., & De La Cruz, E. M. (2013). Regulation of actin by ion-linked equilibria. *Biophys J*, *105*(12), 2621-2628. doi:10.1016/j.bpj.2013.10.032
- Kang, H., Bradley, M. J., McCullough, B. R., Pierre, A., Grintsevich, E. E., Reisler, E., & De La Cruz, E. M. (2012). Identification of cation-binding sites on actin that drive polymerization and modulate bending stiffness. *Proc Natl Acad Sci U S A*, *109*(42), 16923-16927. doi:10.1073/pnas.1211078109
- Koculi, E., Hyeon, C., Thirumalai, D., & Woodson, S. A. (2007). Charge density of divalent metal cations determines RNA stability. *J Am Chem Soc*, *129*(9), 2676-2682. doi:10.1021/ja068027r
- Korkmaz Zirpel, N., & Park, E. J. (2015). Trivalent Cation Induced Bundle Formation of Filamentous fd Phages. *Macromol Biosci*, *15*(9), 1262-1273. doi:10.1002/mabi.201500046
- Lai, G. H., Coridan, R., Zribi, O. V., Golestanian, R., & Wong, G. C. (2007). Evolution of growth modes for polyelectrolyte bundles. *Phys Rev Lett*, *98*(18), 187802. doi:10.1103/PhysRevLett.98.187802
- Li, B.-l., Wang, Y.-f., & Gong, J.-h. (2014). Using a form-finding model to analyze the effect of actin bundles on the stiffness of a cytoskeleton network. *J Zhejiang Univ Sci.*, *15*(9), 732-742.

- Lieleg, O., Kayser, J., Brambilla, G., Cipelletti, L., & Bausch, A. R. (2011). Slow dynamics and internal stress relaxation in bundled cytoskeletal networks. *Nat Mater*, *10*(3), 236-242. doi:10.1038/nmat2939
- MacKerell, A. D., Feig, M., & Brooks, C. L. (2004). Extending the treatment of backbone energetics in protein force fields: Limitations of gas phase quantum mechanics in reproducing protein conformational distributions in molecular dynamics simulations. *J Comput Chem*, *25*(11), 1400-1415.
- McCullough, B. R., Grintsevich, E. E., Chen, C. K., Kang, H., Hutchison, A. L., Henn, A., . . . De La Cruz, E. M. (2011). Cofilin-linked changes in actin filament flexibility promote severing. *Biophys J*, *101*(1), 151-159. doi:10.1016/j.bpj.2011.05.049
- Otterbein, L. R., Graceffa, P., & Dominguez, R. (2001). The crystal structure of uncomplexed actin in the ADP state. *Science*, *293*(5530), 708-711. doi:10.1126/science.1059700
- Phillips, J. C., Braun, R., Wang, W., Gumbart, J., Tajkhorshid, E., Villa, E., . . . Schulten, K. (2005). Scalable molecular dynamics with NAMD. *J Comput Chem*, *26*(16), 1781-1802.
- Pollard, T. D., & Borisy, G. G. (2003). Cellular motility driven by assembly and disassembly of actin filaments. *Cell*, *112*(4), 453-465.
- Pollard, T. D., & Cooper, J. A. (2009). Actin, a central player in cell shape and movement. *Science*, *326*(5957), 1208-1212. doi:10.1126/science.1175862
- Rosin, C., Schummel, P. H., & Winter, R. (2015). Cosolvent and crowding effects on the polymerization kinetics of actin. *Phys. Chem. Chem. Phys.*, *17*(13), 8330-8337.

- Scharf, R. E., & Newman, J. (1995). Mg- and Ca-actin filaments appear virtually identical in steady-state as determined by dynamic light scattering. *Biochim Biophys Acta*, 1253(2), 129-132.
- Stokes, D. L., & DeRosier, D. J. (1991). Growth conditions control the size and order of actin bundles in vitro. *Biophys J*, 59(2), 456-465. doi:10.1016/s0006-3495(91)82239-1
- Takatsuki, H., Bengtsson, E., & Mansson, A. (2014). Persistence length of fascin-cross-linked actin filament bundles in solution and the in vitro motility assay. *Biochim Biophys Acta*, 1840(6), 1933-1942. doi:10.1016/j.bbagen.2014.01.012
- Tang, J. X., Ito, T., Tao, T., Traub, P., & Janmey, P. A. (1997). Opposite effects of electrostatics and steric exclusion on bundle formation by F-actin and other filamentous polyelectrolytes. *Biochemistry*, 36(41), 12600-12607. doi:10.1021/bi9711386
- Tang, J. X., & Janmey, P. A. (1996). The polyelectrolyte nature of F-actin and the mechanism of actin bundle formation. *J Biol Chem*, 271(15), 8556-8563.
- Tobacman, L. S., & Korn, E. D. (1983). The kinetics of actin nucleation and polymerization. *J Biol Chem*, 258(5), 3207-3214.
- Winkelman, J. D., Suarez, C., Hocky, G. M., Harker, A. J., Morganthaler, A. N., Christensen, J. R., . . . Kovar, D. R. (2016). Fascin-and α -Actinin-Bundled Networks Contain Intrinsic Structural Features that Drive Protein Sorting. *Curr. Biol.*, 26(20), 2697-2706.
- Wong, G. C., & Pollack, L. (2010). Electrostatics of strongly charged biological polymers: ion-mediated interactions and self-organization in nucleic acids and proteins. *Annu Rev Phys Chem*, 61, 171-189. doi:10.1146/annurev.physchem.58.032806.104436

- Yang, C., Czech, L., Gerboth, S., Kojima, S.-i., Scita, G., & Svitkina, T. (2007). Novel roles of formin mDia2 in lamellipodia and filopodia formation in motile cells. *PLoS Biol*, 5(11), e317.
- Yu, X., & Carlsson, A. E. (2003). Multiscale study of counterion-induced attraction and bundle formation of F-actin using an Ising-like mean-field model. *Biophys J*, 85(6), 3532-3543. doi:10.1016/s0006-3495(03)74773-0
- Zheng, T., Cherubin, P., Cilenti, L., Teter, K., & Huo, Q. (2016). A simple and fast method to study the hydrodynamic size difference of protein disulfide isomerase in oxidized and reduced form using gold nanoparticles and dynamic light scattering. *Analyst*, 141(3), 934-938.